Check for updates

ARTICLE

SLC1A1-mediated cellular and mitochondrial influx of R-2-hydroxyglutarate in vascular endothelial cells promotes tumor angiogenesis in IDH1-mutant solid tumors

Xiaomin Wang[1,2,9], Ziqi Chen[1,2,9], Jun Xu[1,2,9], Shuai Tang[1,9], Nan An[1,2,9], Lei Jiang[3], Yixiang Zhang[3], Shaoying Zhang[4], Qingli Zhang[5], Yanyan Shen[1], Shijie Chen[1,2], Xiaojing Lan[1], Ting Wang[1,2], Linhui Zhai[1], Siyuwei Cao[1], Siqi Guo[1,2], Yingluo Liu[1,2], Aiwei Bi[1,2], Yuehong Chen[1], Xiameng Gai[1,6], Yichen Duan[1,6], Ying Zheng[1,2], Yixian Fu[1,2], Yize Li[1,2], Liang Yuan[1], Linjiang Tong[1], Kun Mo[7], Mingcheng Wang[1], Shu-Hai Lin [8], Minjia Tan [1,2,6], Cheng Luo[1,2,7], Yi Chen[1,2], Jia Liu [5], Qiansen Zhang[4], Leping Li[3] and Min Huang [1,2,6,7✉]

Mutant isocitrate dehydrogenase 1 (mIDH1) drives tumorigenesis via producing oncometabolite R-2-hydroxyglutarate (R-2-HG) across various tumor types. However, mIDH1 inhibitors appear only effective in hematological tumors. The therapeutic benefit in solid tumors remains elusive, likely due to the complex tumor microenvironment. In this study, we discover that R-2-HG produced by IDH1-mutant tumor cells is preferentially imported into vascular endothelial cells and remodels mitochondrial respiration to promote tumor angiogenesis, conferring a therapeutic vulnerability in IDH1-mutant solid tumors. Mechanistically, SLC1A1, a Na^+-dependent glutamate transporter that is preferentially expressed in endothelial cells, facilitates the influx of R-2-HG from the tumor microenvironment into the endothelial cells as well as the intracellular trafficking of R-2-HG from cytoplasm to mitochondria. R-2-HG hijacks SLC1A1 to promote mitochondrial Na^+/Ca^{2+} exchange, which activates the mitochondrial respiratory chain and fuels vascular endothelial cell migration in tumor angiogenesis. SLC1A1 deficiency in mice abolishes mIDH1-promoted tumor angiogenesis as well as the therapeutic benefit of mIDH1 inhibitor in solid tumors. Moreover, we report that HH2301, a newly discovered mIDH1 inhibitor, shows promising efficacy in treating IDH1-mutant cholangiocarcinoma in preclinical models. Together, we identify a new role of SLC1A1 as a gatekeeper of R-2-HG-mediated crosstalk between IDH1-mutant tumor cells and vascular endothelial cells, and demonstrate the therapeutic potential of mIDH1 inhibitors in treating IDH1-mutant solid tumors via disrupting R-2-HG-promoted tumor angiogenesis.

INTRODUCTION

Isocitrate dehydrogenase 1 (IDH1) gene is frequently mutated in human cancers, in particular in low-grade gliomas, acute myeloid leukemia (AML) and cholangiocarcinoma.[1–4] There has been great enthusiasm in the development of mutant IDH1 (mIDH1) inhibitors, leading to the approval of a first-in-class mIDH1 inhibitor, ivosidenib (AG-120),[5] for the treatment of IDH1-mutant AML. However, the therapeutic benefit of mIDH1 inhibition in solid tumors, despite the high IDH1 mutation frequency, appears elusive. Accumulated preclinical evidence shows that mIDH1 inhibitors did not affect the growth of IDH1-mutant solid tumors, particularly gliomas.[6–8] A recent phase I clinical trial of AG-120 in IDH1-mutant advanced glioma suggests the potential clinical benefit that is worthy of further investigation.[9] To date, the most promise of mIDH1 inhibitors in treating solid tumors was demonstrated in a phase III trial of AG-120 in treating advanced IDH1-mutant cholangiocarcinoma.[10] The modest response in this study has rejuvenated the interest in mIDH1 inhibitors for treating solid tumors. However, mechanistic understanding of the therapeutic response of mIDH1 inhibitors in solid tumors is lacking.

mIDH1 gains an abnormal enzymatic activity that converts α-ketoglutarate (α-KG) to onco-metabolite R-2-hydroxyglutarate (R-2-HG), a major player of the oncogenic activity of mIDH1.[11] The mechanistic understanding of the oncogenic role of R-2-HG within tumor cells has experienced explosive growth in the past decade. R-2-HG is mostly known for its role to inhibit the activity of a variety of α-KG-dependent dioxygenases, many of which function as epigenetic modifiers, resulting in the alteration of epigenomic landscape.[12–14] Recently, emerging evidence has suggested that R-2-HG may confer growth advantages to tumor cells through

[1]State Key Laboratory of Drug Research, Shanghai Institute of Materia Medica, Chinese Academy of Sciences, Shanghai, China. [2]University of Chinese Academy of Sciences, Beijing, China. [3]Haihe Biopharma, Shanghai, China. [4]Shanghai Key Laboratory of Regulatory Biology, Institute of Biomedical Sciences, School of Life Sciences, East China Normal University, Shanghai, China. [5]Shanghai Institute of Materia Medica, Chinese Academy of Sciences, Shanghai, China. [6]School of Chinese Materia Medica, Nanjing University of Chinese Medicine, Nanjing, Jiangsu, China. [7]School of Pharmaceutical Science and Technology, Hangzhou Institute for Advanced Study, University of Chinese Academy of Sciences, Hangzhou, Zhejiang, China. [8]State Key Laboratory of Cellular Stress Biology, School of Life Sciences, National Institute for Data Science in Health and Medicine, Xiamen University, Xiamen, Fujian, China. [9]These authors contributed equally: Xiaomin Wang, Ziqi Chen, Jun Xu, Shuai Tang, Nan An. ✉email: mhuang@simm.ac.cn
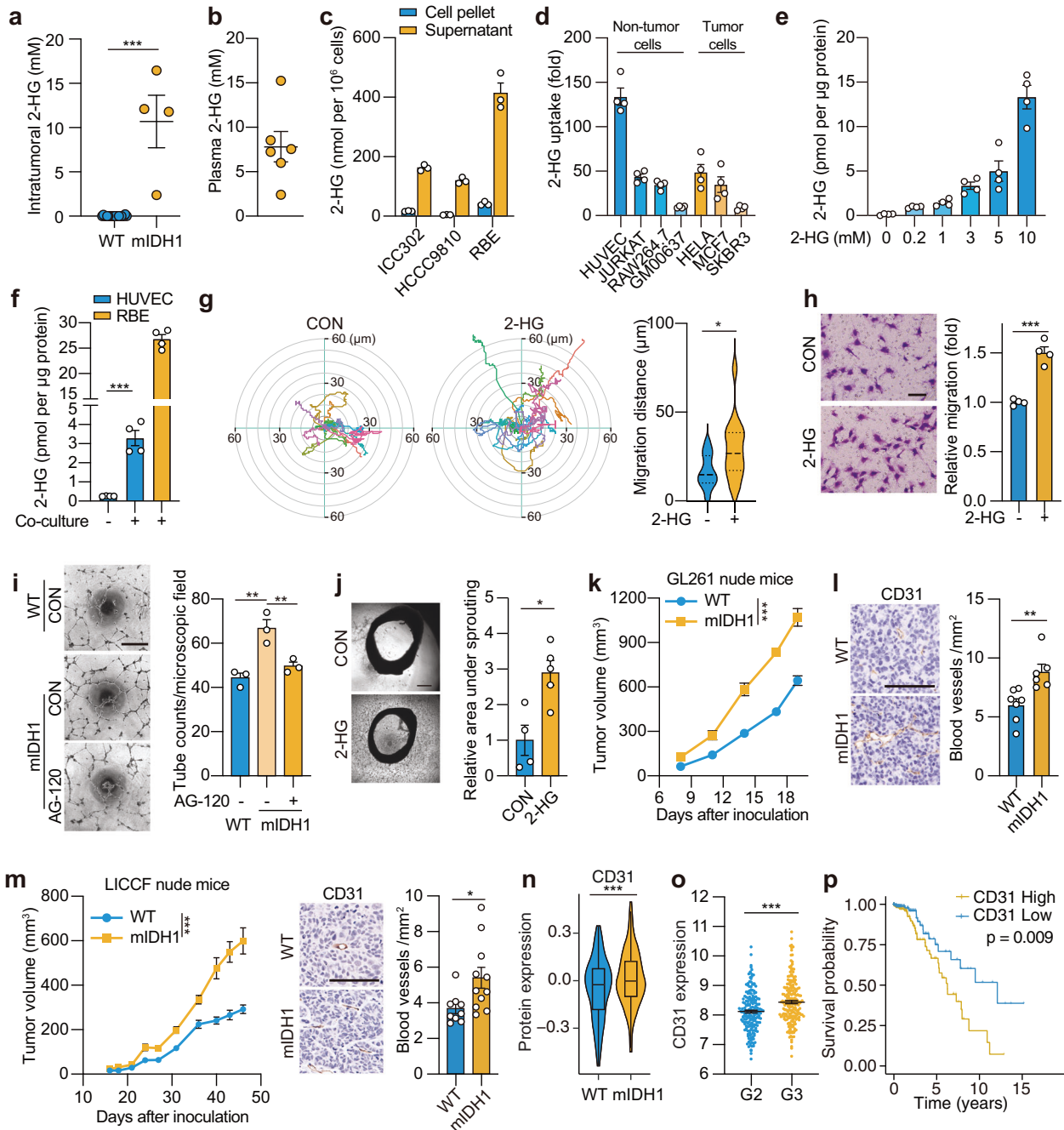
non-tumor cell-autonomous effects,[15,16] yet the precise mechanism remains unclear. A better understanding of the role of R-2-HG in the tumor microenvironment may provide important insights for applying mIDH1 inhibitors to treat solid tumors.

To establish the role of R-2-HG in the tumor microenvironment, a fundamental question is how highly hydrophilic R-2-HG, a dicarboxylate, overcomes the hurdle of hydrophobic membranes to transport between tumor cells and surrounding cells.[13,16] This question raises a speculation that the expression of transmembrane transporters, serving as the "metabolic gatekeeper" of cells, may account for a regulatory mechanism underlying R-2-HG-mediated cell crosstalk in the tumor microenvironment. In particular, the heterogeneous expression of transmembrane

transporters may provide explanations for the divergent roles of R-2-HG that are increasingly noted in different cell contexts.[15,16]

This study aimed to gain the mechanistic insights into the role of R-2-HG in the tumor microenvironment and to explore therapeutic implications of mIDH1 inhibitors in treating solid tumors. We here identify SLC1A1, a Na^+-dependent glutamate transporter that is preferentially expressed in endothelial cells as a gatekeeper to orchestrate R-2-HG-mediated tumor–endothelial cell crosstalk in regulating tumor angiogenesis. In addition, we also show that, HH2301, a novel mIDH1 inhibitor, exhibits the profound advantage in treating IDH1-mutant cholangiocarcinoma compared with AG-120, due to the improved potency in disrupting R-2-HG-promoted angiogenesis.

Fig. 1 R-2-HG influx promotes vascular endothelial cell migration. a R-2-HG concentration in patient-derived cholangiocarcinoma samples. $n = 20$ for WT; $n = 4$ for mIDH1. **b** Serum R-2-HG concentration. IDH1-mutant patient tumors as described in **a** were implanted into nude mice ($n = 6$). **c** R-2-HG amount in the supernatant or cell pellets of cholangiocarcinoma cells. Cells were cultured for 48 h before collecting the indicated samples for R-2-HG analysis. R-2-HG amount was normalized by cell numbers. **d** R-2-HG uptake in a panel of cells representing cell components in the tumor microenvironment. Cells were treated with R-2-HG (10 mM) for 1 h. **e** R-2-HG uptake by vascular endothelial cells. HUVECs were treated with R-2-HG at indicated concentrations and intracellular R-2-HG amount was normalized by the protein amount. **f** The uptake of tumor cell-derived R-2-HG by HUVECs. RBE cells were co-cultured with HUVECs for 1 h. Intracellular R-2-HG amount was measured. **g** Time-lapse analysis of cell-motility. HUVECs were treated with R-2-HG (10 mM) and images were captured for 4 h. Left, representative cell traces with migration origin superimposed at the zero-cross point; Right, quantification of migration distance ($n > 10$). **h** Transwell migration assay. HUVECs were treated with R-2-HG (10 mM) for 24 h. Shown were representative images of migrated cells and quantification. Scale bar, 100 μm. **i** Tube formation assay. HUVECs were cultured with conditioned medium from GL261 cells overexpressing WT or mIDH1 and treated with AG-120 (1 μM) for 6 h. Shown were representative images of tube formation and quantification. Scale bar, 200 μm. **j** Aortic ring sprouting assay. Matrigel-ring mixture was treated with R-2-HG (10 mM) for 7 days. Shown were representative images and quantification of aortic ring sprouting. Scale bar, 500 μm. **k, l** Tumor growth curve and tumor blood vessel density. GL261-WT and -mIDH1 cells were inoculated into nude mice ($n = 7$ for WT; $n = 6$ for mIDH1) and tumor tissues were subjected to immunohistochemistry analysis. Shown were representative images of CD31 staining and quantification. Scale bar, 100 μm. **m** Tumor growth curve and blood vessel density of LICCF-WT and -mIDH1 tumors in nude mice ($n = 9$ for WT; $n = 11$ for mIDH1). Scale bar, 100 μm. **n** CD31 protein level in 283 low grade glioma with or without IDH1 mutation extracted from TCGA database. **o** CD31 mRNA expression levels between different histologic grade tumors in IDH1-mutant subset. **p** Survival analysis among CD31 high- and low-expression patients. The same set of data as in **o** were used for the analysis. For all graphs, data in **c–j** represent means of indicated technical replicates and data in **a, b, l, m, n** and **o** represent means of individual tumors or mice; error bars represent SEM. Statistical analyses were performed using Student's t-test for **a, f–h** and **j–o**, one-way ANOVA for **i**, and Log-rank test for **p**. *$P <$ 0.05, **$P < 0.01$, ***$P < 0.001$.

RESULTS
Extracellular R-2-HG is preferentially imported to vascular endothelial cells to promote tumor angiogenesis

IDH1-mutant tumor cells, despite tissue of origin, are similarly characterized by the massive production of R-2-HG. To understand how R-2-HG accumulation affects the tumor microenvironment, we firstly measured R-2-HG concentration in a collection of 24 patient-derived cholangiocarcinoma tissues, among which four samples harbor IDH1-R132C mutation. Consistent with previous findings,[11,16,17] Enormous amount of R-2-HG was detected in IDH1-mutant tumor samples (Fig. 1a), with an average concentration of approximately 10 mM (ranged from 3 to 18 mM). Implantation of patient-derived tumors in nude mice gave rise to the serum R-2-HG concentration comparable to that of tumor tissues (Fig. 1b). As it remains technically challenging to directly measure the interstitial R-2-HG amount in the tumor microenvironment, we measured R-2-HG amount in the supernatant and cell pellets from IDH1-mutant cholangiocarcinoma cell culture, to roughly reflect the situation in the tumor microenvironment. After 48-h culture, R-2-HG amount in the culture media was up to 20-fold of that within the cells (Fig. 1c), suggesting the rapid accumulation of R-2-HG in the tumor microenvironment, mainly in the tumor stroma. Given the average R-2-HG concentration in whole tumor mass is around 10 mM, we speculate that the interstitial R-2-HG accumulated in the tumor microenvironment would easily reach 10 mM and even higher.

To evaluate whether the extracellular R-2-HG could be taken up by cells in the tumor microenvironment, R-2-HG at a pathologically relevant concentration (10 mM) was directly added into the culture of a panel of cell lines widely used to represent the major cell components in tumor tissues, including immune cells, vascular endothelial cells and fibroblasts. Tumor cells originated from different tissue types were used as controls. We discovered that R-2-HG could be differentially imported into these cells, among which the primary human umbilical vein endothelial cells (HUVECs) showed a remarkably high level of R-2-HG influx (Fig. 1d), suggesting the preferential uptake of R-2-HG by vascular endothelial cells. HUVECs exposed to gradient concentrations of R-2-HG showed dose-dependent R-2-HG uptake (Fig. 1e). To exclude that the observed R-2-HG increase was due to the stimulated intracellular R-2-HG production, [U-^{13}C$_5$]-labeled R-2-HG tracing was performed, and the result confirmed the transportation of extracellular R-2-HG into HUVECs (Supplementary information, Fig. S1a). Active R-2-HG uptake by vascular endothelial cells was also confirmed in primary human retinal

endothelial cells (HRECs) (Supplementary information, Fig. S1b). Further, we carried out a co-culture experiment using HUVECs and IDH1-mutant cholangiocarcinoma REB cells, and confirmed the uptake of tumor-originated R-2-HG by HUVECs (Fig. 1f). Of note, the resultant intracellular concentration of R-2-HG in HUVECs was much lower than that in REB cells (Fig. 1f), suggesting that compared with tumor cells bearing autonomous IDH1 mutation, intracellular R-2-HG in non-tumor cells is at a relatively low level.

We next asked whether the limited R-2-HG uptake could cause functional change in HUVECs. Endothelial cells are central players in tumor angiogenesis, a process of blood vessel sprouting from existing tumor vessels essentially involved in the progression and metastasis of solid tumors.[18,19] A recent study reported the enhanced vascular endothelial cell growth stimulated by the treatment of R-2-HG at sub-millimolar concentrations, much lower than R-2-HG concentrations in human tumor tissues.[20] However, at pathologically relevant concentrations (3–10 mM), we did not observe the significant impact of R-2-HG on endothelial cell growth (Supplementary information, Fig. S1c). This result was further confirmed by co-culturing HUVECs with a constructed murine glioblastoma cell line Glioma 261 (GL261) expressing human wild-type IDH1 (GL261-WT) or mIDH1 (GL261-mIDH1) (Supplementary information, Fig. S1d, e), largely ruling out the impact on cell growth.

As vascular sprouting relies on the coordinated activity of both migrating tip cells at the forefront and proliferating stalk cells that elongate the sprout,[21] we next assessed the impact of R-2-HG on the mobility of endothelial cells. A time-lapse analysis of single cell mobility showed that R-2-HG treatment enhanced the mobility of HUVECs (Fig. 1g). These findings were confirmed using widely-applied approaches for assessing cell mobility change, the wound-healing assay (Supplementary information, Fig. S1f) and the transwell migration assay (Fig. 1h). Treatment of HRECs with R-2-HG similarly enhanced cell migration (Supplementary information, Fig. S1g). Further, the tube formation assay was applied to simulate the reorganization stage of angiogenesis.[22] R-2-HG treatment increased lumen-forming ability of endothelial cells (Supplementary information, Fig. S1h). Consistently, HUVECs exposed to conditioned medium from GL261-mIDH1 cells showed the elevated lumen-forming ability compared with those exposed to GL261-WT-conditioned medium, and this difference could be reversed by the inhibition of mIDH1 enzymatic activity using AG-120 (Fig. 1i; Supplementary information, Fig. S1i, j). Moreover, HUVECs co-cultured with GL261-WT cells and treated with R-2-HG recapitulated the phenotype of those co-cultured with GL261-
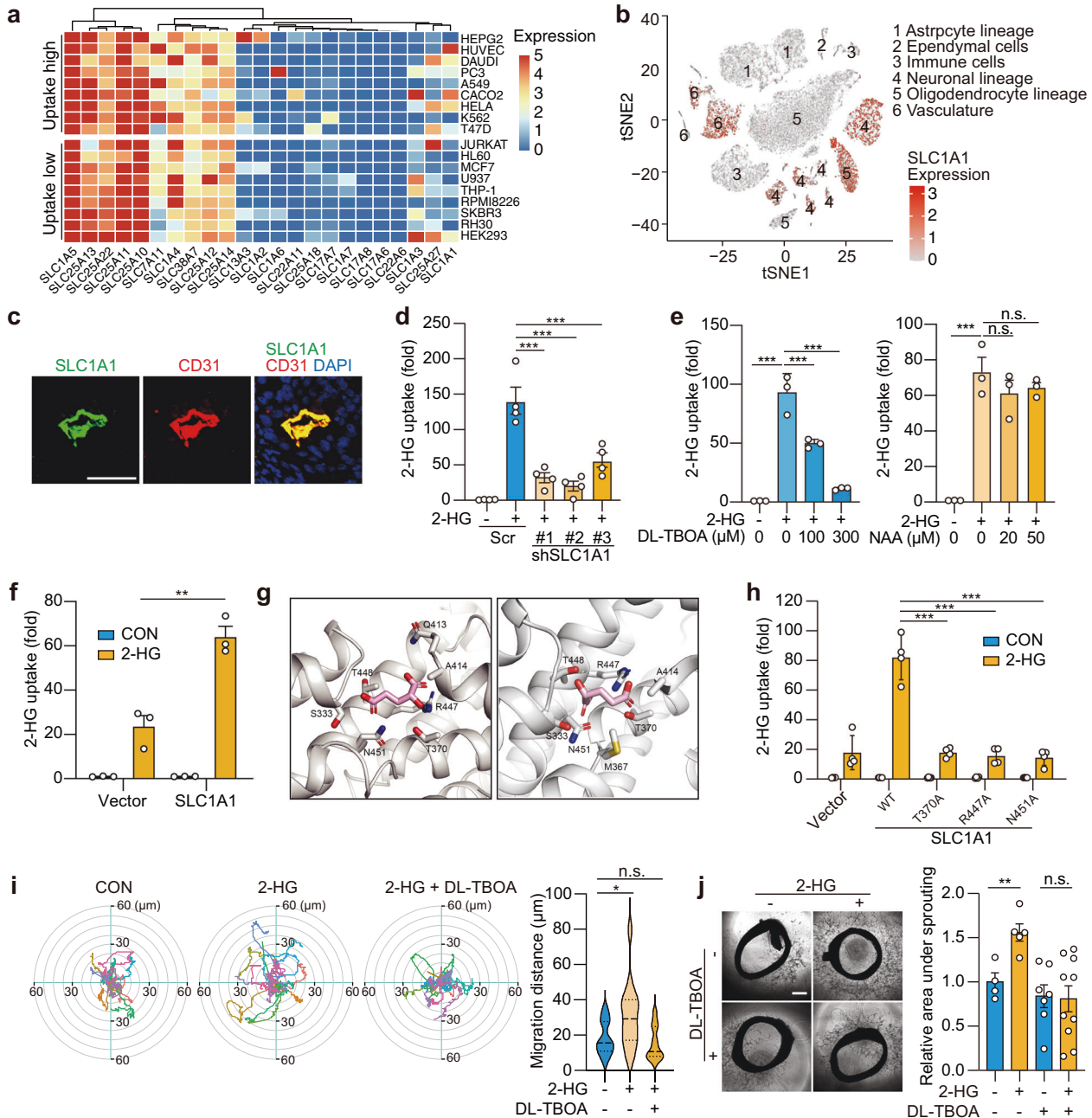
Fig. 2 SLC1A1-dependent R-2-HG uptake by vascular endothelial cells. a Heatmap of mRNA expression of SLC transporters. Cells were divided into high- and low-uptake groups based on median fold change (cutoff = 45) of R-2-HG uptake. Expressions of SLC transporters were extracted from Human Protein Atlas and CCLE databases. **b** Single-cell sequencing of normal brain tissues showing cell-type-dependent SLC1A1 expression. Data were extracted from the Single Cell Portal database. **c** *SLC1A1* expression in cholangiocarcinoma patient-derived xenograft (PDX) tissues. *SLC1A1* and *CD31* expression was examined using RNA FISH analysis. Scale bar, 50 µm. **d** The impact of SLC1A1 depletion on R-2-HG uptake. HUVECs were transduced with indicated shRNAs for 72 h and then exposed to R-2-HG (10 mM) for 1 h. **e** The impact of SLC1A1 inhibitor on R-2-HG uptake. HUVECs were pre-treated with DL-TBOA or NAA at indicated concentrations for 1 h and then exposed to R-2-HG (10 mM) for 1 h. **f** The impact of SLC1A1 overexpression on R-2-HG uptake. 293T cells transfected with indicated plasmids for 72 h were treated as assay shown in **d**. **g** The binding sites of R-2-HG to SLC1A1 in the outward-occluded (left) and inward-occluded (right) states. Critical side chains of R-2-HG were shown as stick. **h** The impact of SLC1A1 mutagenesis on R-2-HG uptake. 293T cells transfected with indicated plasmids for 72 h were treated as assay shown in **d**. **i** Time-lapse analysis of cell-motility. HUVECs were treated with R-2-HG (10 mM) alone or in combination with DL-TBOA (300 µM) and images were captured for 4 h. Left, representative cell traces with migration origin superimposed at the zero-cross point; Right, quantification of migration distance (*n* > 10). **j** Aortic ring sprouting assay. Matrigel-ring mixture was treated with R-2-HG (10 mM) alone or in combination with DL-TBOA (300 µM) for 7 days. Shown were representative images and quantification of aortic ring sprouting. Scale bar, 500 µm. All data represent means of indicated technical replicates; error bars represent SEM. Statistical analyses were performed using Student's *t*-test for **f** and **j**, and one-way ANOVA for **d**, **e**, **h** and **i**. ns, not significant. *$P < 0.05$, **$P < 0.01$, ***$P < 0.001$.
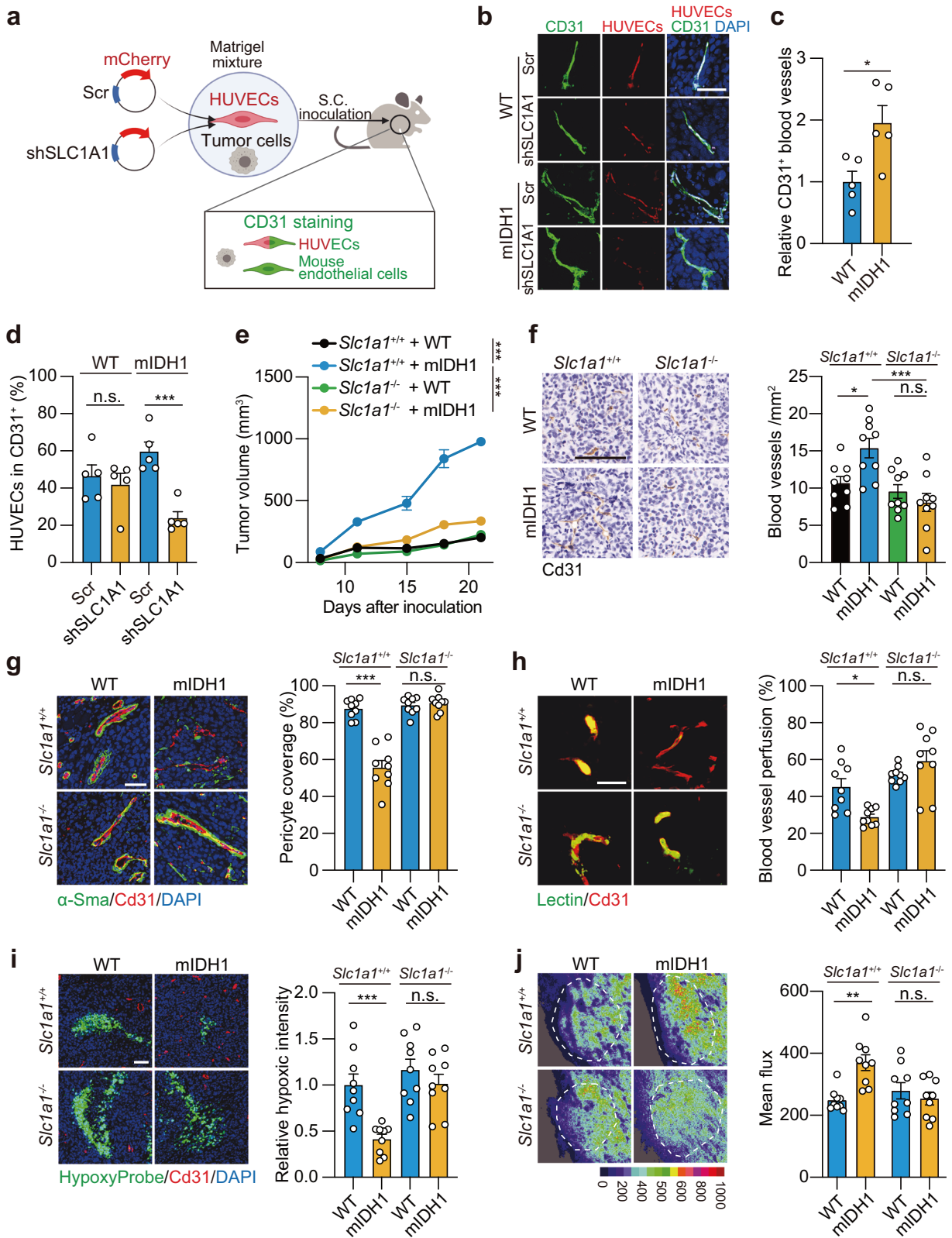
mIDH1 cells (Supplementary information, Fig. S1k), largely ruling out the possibility of the involvement of other tumor-derived factors in promoting angiogenesis. Further, a three-dimensional rat aortic ring assay that is believed to mimic the complexities of angiogenesis in vivo was applied. The result revealed the

substantially improved sprouting of aortic ring upon R-2-HG treatment (Fig. 1j).

We next confirmed these findings in vivo. To this end, GL261-WT and GL261-mIDH1 cells were inoculated into C57BL/6 mice. GL261-mIDH1 tumors exhibited the promoted tumor growth

Fig. 3 SLC1A1 deficiency impedes R-2-HG-promoted tumor angiogenesis. a–d In vivo vessel formation of HUVECs. HUVECs infected with mCherry-lentivirus expressing Scr or shSLC1A1 were mixed with GL261-WT or -mIDH1 cells in matrigel and then implanted into nude mice ($n = 5$). **a** Scheme of experimental procedure. **b** Representative images of CD31 immunofluorescence staining and vessels with mCherry marker. Scale bar, 50 μm. **c** Quantification of total CD31-positive vessels. Shown were groups co-implanted with HUVECs-Scr. **d** Ratios of mCherry-positive vessels to total CD31-positive vessels. **e** Tumor growth curve. GL261-WT and -mIDH1 cells were inoculated into wild-type (SLC1A1$^{+/+}$) or SLC1A1$^{-/-}$ C57BL/6 mice ($n = 9$). **f** Blood vessel density in tumor tissues. Tumor tissues from assay in **e** were subjected to immunohistochemistry analysis. Shown were representative images of CD31 staining and quantification. Scale bar, 100 μm. **g** Pericyte coverage of tumor vasculature. Tumor tissues from assay in **e** were subjected to immunofluorescence staining using anti-α-SMA (green) and anti-CD31 (red) antibodies. Shown were representative images and quantification of α-SMA-positive vessels in total vessels. Scale bar, 50 μm. **h** Tumor vascular perfusion. Mice used in **e** were intravenously injected with FITC-lectin (green) before tumors were collected. Tumor blood vessels were visualized by CD31 staining (red). Shown were representative images and quantification of lectin-positive vessels in total vessels. Scale bar, 50 μm. **i** Tumor hypoxia analysis. Mice used in **e** were intravenously injected with pimonidazole hydrochloride before tumors were collected. Tumor tissues were subjected to immunofluorescence staining using Hypoxyprobe-1-Mab1 FITC (green) and anti-CD31 (red) antibodies. Shown were representative images and quantification of the fluorescence intensity of Hypoxyprobe. Scale bar, 50 μm. **j** Blood flow measured using FLPI in anaesthetized mice from assay in **e**. Shown were representative images of blood flow and quantification. Tumor areas were indicated by dashed lines. All data represent means of individual mice; error bars represent SEM. Statistical analyses were performed using Student's t-test for **c–e** and **g–j**, and one-way ANOVA for **f**. ns, not significant. *$P < 0.05$, **$P < 0.01$, ***$P < 0.001$.

compared with the wild-type counterpart (Supplementary information, Fig. S1l), in great contrast to cell proliferation in vitro that the two cell lines grew similarly (Supplementary information, Fig. S1m). The promoted tumor growth of GL261-mIDH1 was associated with a higher intratumoral blood vessel intensity, as revealed by CD31 staining (Supplementary information, Fig. S1n). Given the reported roles of R-2-HG in modulating the anti-tumor immunity,[15,16] tumor growth of these cells was also examined in immune-deficient nude mice. GL261-mIDH1 tumors exhibited significantly enhanced tumor growth and angiogenesis compared with GL261-WT tumors (Fig. 1k, l), though the difference in tumor growth was less striking compared with that in immune-competent C57BL/6 mice (Fig. 1k; Supplementary information, Fig. S1l). Similar findings were obtained in another pair of cholangiocarcinoma LICCF cells expressing IDH1-WT (LICCF-WT) or mIDH1 (Fig. 1m; Supplementary information, Fig. S1o, p). These results suggest that R-2-HG could promote tumor growth and angiogenesis independent of its impact on immune cells.

We further explored patient samples from TCGA database. Intratumoral blood vessels were examined in lower grade glioma (LGG) known for the high IDH1 mutation frequency. Tumors with mIDH1 ($n = 217$) showed higher levels of vascular endothelial marker CD31 as compared with wild-type tumors ($n = 66$) (Fig. 1n), suggesting the association between IDH1 mutation and the increased tumor angiogenesis. Among IDH1-mutant patients, CD31 expression was associated with the tumor progression (Fig. 1o) and the patient survival (Fig. 1p).

The aforementioned results together suggest that R-2-HG originated from IDH1-mutant tumor cells promotes tumor angiogenesis and tumor growth via enhancing the mobility of vascular endothelial cells.

R-2-HG is transported into vascular endothelial cells by SLC1A1

Metabolite transporters serve as gatekeepers to facilitate the metabolic crosstalk between tumor cells and the microenvironment. Previous studies have reported that solute carrier (SLC) family transporters SLC13A3, SLC22A6 and SLC22A11 are responsible for transporting R-2-HG in different cell context,[16] yet these transporters are expressed at an extremely low level in HUVECs (Supplementary information, Fig. S2a), suggesting the involvement of alternative transporters. To identify new R-2-HG transporters, we analyzed the correlation between the expression of SLC transporters and R-2-HG uptake in 18 cell lines that were subgrouped into two subsets (uptake high/low) according to R-2-HG uptake activity (median intracellular R-2-HG fold change = 45 as cutoff) (Supplementary information, Fig. S2b). Considering the chemical property of R-2-HG, dicarboxylic acid and glutamate transporters were examined and their expression levels were

extracted from Human Protein Atlas and Cancer Cell Line Encyclopedia (CCLE) databases. The results revealed a close association between the extent of R-2-HG uptake and the expression of SLC1A1, a Na$^+$-dependent glutamate transporter also known as EAAC1 (Fig. 2a; Supplementary information, Fig. S2c and Table S1).

SLC1A1 is mostly known as a neuronal glutamate transporter involved in neuropsychiatric disorders.[23] To understand the potential role of SLC1A1 in endothelial cells, we looked into the intrinsic SLC1A1 expression in different cell types. Single-cell sequencing analysis of brain tissue from the Single Cell Portal database[24] revealed that the expression of SLC1A1 in endothelial cells is abundant and comparable to that in cells of neuronal lineage, but much higher than that in the rest cell types (Fig. 2b). These findings were echoed by SLC1A1 mRNA (Supplementary information, Fig. S2d) and protein (Supplementary information, Fig. S2e) expression data among cell lines of different tissue origins. Further, fluorescence staining of patient-derived cholangiocarcinoma tissues revealed a specific expression of SLC1A1 in CD31-positive vascular endothelial cells (Fig. 2c), all implying a role of SLC1A1 in vascular endothelial cells in the tumor microenvironment.

Next, we examined whether SLC1A1 is responsible for R-2-HG uptake in HUVECs. Knockdown of SLC1A1 significantly reduced R-2-HG influx into HUVECs (Fig. 2d; Supplementary information, Fig. S2f). Likewise, pretreatment of DL-TBOA, a pharmacological inhibitor of SLC1A1, dose-dependently inhibited R-2-HG uptake. As a negative control, N-(P-amylcinnamoyl) anthranilic acid (NAA), an inhibitor of SLC13A3 that was reported to inhibit R-2-HG influx in T cells,[16] did not show the noticeable effect (Fig. 2e). Further, ectopic expression of SLC1A1 in 293T cells that barely express endogenous SLC1A1 enhanced R-2-HG uptake (Fig. 2f; Supplementary information, Fig. S2g). These results suggest that SLC1A1 is mainly, if not solely, responsible for R-2-HG influx in vascular endothelial cells. We also tested whether SLC1A1 is able to transport R-2-HG out of cells. To this end, SLC1A1 was introduced into IDH1-mutant REB and HT1080 tumor cells, both producing enormous amount of R-2-HG. However, ectopic expression of SLC1A1 did not increase R-2-HG export (Supplementary information, Fig. S2h), largely excluding its role in R-2-HG export.

To understand how SLC1A1 mechanistically transports R-2-HG, we took an approach of molecular modeling and docking analysis. SLC1A1 models were built based on the structures of the alanine serine cysteine transporter 2 (ASCT2, also shown as SLC1A5), a homolog of SLC1A1 with sequences highly conserved in the substrate binding sites (Supplementary information, Fig. S2i), and its structures in complex with glutamine in the outward-occluded and inward-occluded states.[25,26] R-2-HG was docked into the pockets of SLC1A1 structural models. In the outward-occluded
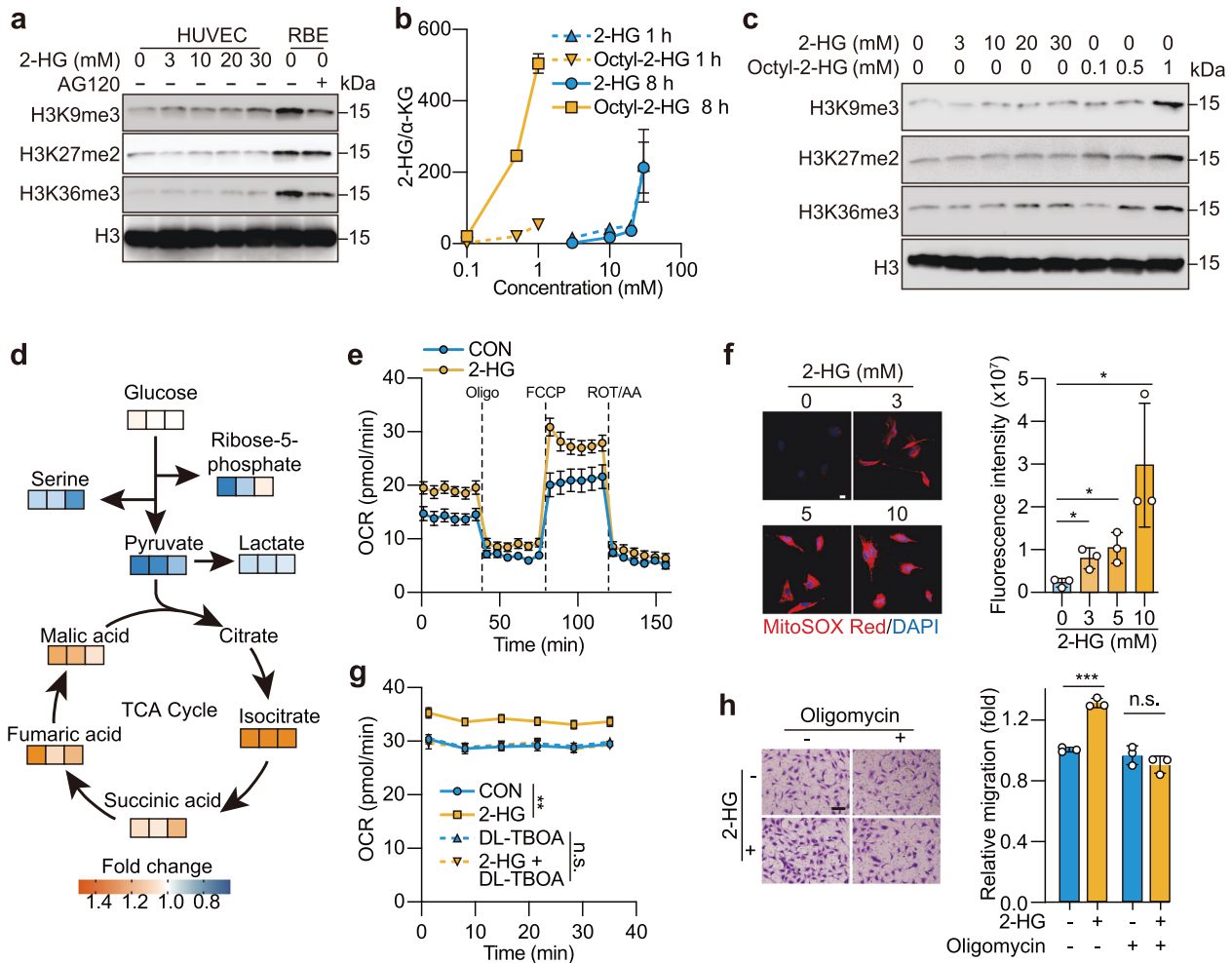
Fig. 4 Restrained R-2-HG uptake activates mitochondrial respiration in vascular endothelial cells. a The impact of R-2-HG on histone methylation. HUVECs were treated with R-2-HG (10 mM) for 8 h. RBE cells treated without or with AG-120 (1 μM, 72 h) were used as positive controls. Specified histone methylation levels were examined by immunoblotting. **b** Ratios of R-2-HG to α-KG in HUVECs. HUVECs were treated with Octyl-R-2-HG (0.1, 0.5 and 1 mM) or R-2-HG (3, 10, 20, 30 mM) for indicated time. Intracellular R-2-HG and α-KG amount was measured. **c** The impact of R-2-HG and Octyl-R-2-HG on histone methylation. HUVECs were treated as indicated for 8 h. **d** Schematic representation of metabolic changes in HUVECs treated with R-2-HG (3 mM) for 8 h. Fold change of metabolites versus untreated group were plotted as heatmap inserts ($n = 3$). Yellow, increased; Blue, decreased. **e** Oxygen consumption rate (OCR) measurement. HUVECs were pre-treated with R-2-HG (10 mM) for 1 h. Oligomycin (Oligo, 2 μM), FCCP (1 μM) and rotenone/antimycin (ROT/AA, 0.5 μM) were added as indicated. **f** Mitochondrial ROS staining. HUVECs were treated with R-2-HG at indicated concentrations for 1 h. Mitochondrial ROS was probed using MitoSox Red. Shown were representative images and quantification. Scale bar, 10 μm. **g** OCR measurement. HUVECs were treated with R-2-HG (10 mM) plus DL-TBOA (300 μM) for 1 h. **h** Transwell migration assay. HUVECs were treated with R-2-HG (10 mM) alone or in combination with oligomycin (2 μM) for 24 h. Shown were representative images of migrated cells and quantification. Scale bar, 100 μm. All images were representative results from at least three independent experiments. Seahorse analysis were performed in 4–8 technical replicates. All data represent means of indicated technical replicates; error bars represent SEM. Statistical analyses were performed using Student's t-test for **g** and **h**, and one-way ANOVA for **f**. ns, not significant. *$P < 0.05$, **$P < 0.01$, ***$P < 0.001$.

state, R-2-HG interacted with S333, T370, Q413, A414, R447 and N451 of SLC1A1, while in the inward-occluded state, R-2-HG interacted with S333, T370, A414, R447 and T448 (Fig. 2g; Supplementary information, Fig. S2j). Among these residues, T370, R447 and N451 were also required for SLC1A1-mediated glutamate transportation.[27] To confirm this model, we applied mutagenesis to T370, R447 and N451 residues. The expression of these mutants in 293T cells substantially impaired SLC1A1-mediated R-2-HG uptake (Fig. 2h; Supplementary information, Fig. S2k, l). In addition, pre-inhibition of SLC1A1 by DL-TBOA blocked R-2-HG-promoted cell mobility (Fig. 2i), cell migration (Supplementary information, Fig. S2m) as well as the three-dimensional rat aortic ring angiogenesis (Fig. 2j). All these results support SLC1A1 as a new R-2-HG transporter that plays an essential role in R-2-HG uptake in vascular endothelial cells.

SLC1A1 is required for R-2-HG-promoted tumor angiogenesis and tumor growth in vivo
We next investigated whether SLC1A1 is functionally required for R-2-HG-promoted tumor angiogenesis in vivo. Firstly, an in vivo vascular network forming assay was performed. In this assay, HUVECs were infected with mCherry lentivirus carrying scramble (Scr) control or SLC1A1 shRNA (shSLC1A1) (Fig. 3a; Supplementary information, Fig. S3a), and then co-implanted with GL261-mIDH1 or GL261-WT cells into nude mice. Total blood vessels were visualized by CD31 staining, among which HUVECs were differentiated by mCherry marker (Fig. 3a). Consistent with results mentioned above, while total blood vessels were increased in GL261-mIDH1 tumors compared with those in GL261-WT tumors (Fig. 3b, c), SLC1A1 depletion in HUVECs significantly decreased the vessel formation of HUVECs, as indicated by CD31/mCherry

dual-positive vessels (Fig. 3b–d; Supplementary information, Fig. S3b). Similar result was obtained by co-implanting mCherry-positive HUVECs with IDH1-mutant cholangiocarcinoma RBE cells (Supplementary information, Fig. S3c, d).

For further confirmation, we generated SLC1A1 knockout mice and implanted GL261-mIDH1 and GL261-WT cell pair into SLC1A1 knockout and wild-type mice in parallel. Of note, mIDH1-promoted tumor growth was largely impeded in SLC1A1-deficient mice as compared with WT mice, suggesting that SLC1A1 is required for mIDH1-conferred growth advantage (Fig. 3e). CD31 staining of tumor tissues showed that blood vessel number was increased in IDH1-mutant tumors as compared to the wild-type counterpart, yet this difference was abolished in SLC1A1-deficient mice (Fig. 3f). Tumor angiogenesis creates an abnormal vascular network characterized by disorganized, immature and permeable blood vessels with poor perfusion.[28,29] To better characterize the role of SLC1A1 in R-2-HG-promoted tumor angiogenesis, we analyzed the tumor vasculature in these mice. As expected, mIDH1 tumor blood vessels showed the decreased coverage with pericyte and collagen, as indicated by α-smooth muscle-actin (α-SMA) and collagen IV (COL IV) staining, which was restored to a level comparable to that in wild-type tumors in SLC1A1-deficient mice (Fig. 3g; Supplementary Fig. 3e). Similar results were observed for vascular perfusion, as visualized by FITC-conjugated lectin (Fig. 3h). These data suggest that IDH1 mutation promotes the vascular abnormality in a SLC1A1-dependent manner. To further evaluate the functional outcome of the blood vessel number change and vasculature abnormality that occurred in parallel, we measured tumor hypoxia. Interestingly, tumor hypoxia was lessened in mIDH1 tumors and this change was abolished in SLC1A1-knockout mice (Fig. 3i). This result suggests that the substantial increase of blood vessels, despite the partially impaired vascular perfusion, facilitates the oxygen supply in mIDH1 tumors. Consistent with this speculation, Doppler laser blood flow analysis revealed the enhanced tumor blood flow in mIDH1 tumors compared with the wild-type counterpart and this difference was eliminated in SLC1A1-knockout mice (Fig. 3j). All these data support that SLC1A1 plays an important role in mIDH1-promoted tumor angiogenesis and tumor growth.

Restrained intracellular uptake of R-2-HG underlies a divergent role in promoting mitochondrial respiration in vascular endothelial cells

We next asked how R-2-HG enhanced the mobility of endothelial cells. It is widely accepted that the oncogenic activity of R-2-HG is mainly through the competitive inhibition of multiple α-KG-dependent dioxygenases, due to the extensive structural similarity between R-2-HG and α-KG. These effects generate genome-wide epigenetic alterations[13] as well as the activation of the hypoxia-inducible factor 1 subunit alpha (HIF-1α)/vascular endothelial growth factor receptor (VEGFR) signaling,[20,30] both of which could contribute to tumor angiogenesis. However, immunoblotting analysis did not find the upregulation of HIF-1α (a slight reduction instead) or VEGFR signaling in HUVECs upon R-2-HG treatment (Supplementary information, Fig. S4a, b). Likewise, histone methylation at H3K9, H3K27 and H3K36, epigenetic markers potentially affected by R-2-HG,[13] were barely affected upon R-2-HG treatment for 8 h (Fig. 4a). In agreement with this result, RNA-seq analysis for up to 48 h treatment (data not shown for 8 h treatment) of R-2-HG did not observe the apparent transcriptional change (Supplementary information, Fig. S4c and Table S2), further ruling out the apparent epigenetic alterations.

Our findings above echoed the increasing evidence that reveals the differential impacts of R-2-HG between tumor and non-tumor cells.[15,16] We speculated that this difference was likely due to the limited intracellular concentration of R-2-HG in non-tumor cells, resulting in disadvantages in competing with α-KG.[13] To test this hypothesis, we measured R-2-HG/α-KG ratios in HUVECs upon R-2-HG treatment. Octyl-R-2-HG, a membrane-permeant derivative of R-2-HG, was used as a control. As expected, R-2-HG treatment at physiologically-relevant concentrations (3–30 mM) elevated the intracellular R-2-HG/α-KG ratios, yet the levels were much lower compared with that caused by Octyl-R-2-HG treatment with even lower dose (1 mM) (Fig. 4b). In particular, Octyl-R-2-HG rather than R-2-HG treatment could cause a time-dependent R-2-HG accumulation within the cells, giving rise to a R-2-HG/α-KG ratio up to 500 folds. This difference is probably due to the continuous conversion of Octyl-R-2-HG to R-2-HG within the cells, which preserves the concentration gradient of Octyl-R-2-HG across the plasma membrane and allows constant diffusion into HUVECs (Fig. 4b). This difference was closely associated with the alterations in H3K9, H3K27 and H3K36 methylation[13] in HUVECs (Fig. 4c). These results provide molecular basis for understanding different mechanisms underlying the function of R-2-HG in different cell context, suggesting a new molecular mechanism of R-2-HG in non-tumor cells.

As R-2-HG production is often associated with metabolic alterations,[6,31,32] we next analyzed the metabolome change of HUVECs using mass spectrometry. Overall, R-2-HG-caused metabolome change was modest. Among 138 identified metabolites, the level of 15 metabolites was elevated by R-2-HG treatment (Supplementary information, Table S3). Pathway analysis of elevated metabolites (cutoff at 1.2-fold) identified the tricarboxylic acid cycle (TCA cycle) as the only pathway significantly affected by R-2-HG (Fig. 4d; Supplementary information, Fig. S4d). Further, Seahorse analysis confirmed that R-2-HG treatment enhanced mitochondrial respiration (Fig. 4e; Supplementary information, Fig. S4e) without affecting the glycolytic capacity in HUVECs (Supplementary information, Fig. S4f). These findings were recapitulated in HRECs (Supplementary information, Fig. S4g, h). MitoSOX staining of mitochondrial ROS production (Fig. 4f) supported the increased mitochondrial respiration stimulated by R-2-HG.

To test whether R-2-HG influx is required for the activation of mitochondrial respiration, SLC1A1 was pre-inhibited by DL-TBOA in HUVECs, which abrogated R-2-HG-activated mitochondrial respiration (Fig. 4g). Further, when mitochondrial respiration chain was impaired by oligomycin prior to R-2-HG treatment, the impact of R-2-HG on cell migration was substantially attenuated as well (Fig. 4h), suggesting that mitochondrial respiration is required for R-2-HG-triggered endothelial cell mobility change.

These results suggest a different mechanism underlying the function of R-2-HG in endothelial cells compared with tumor cells bearing endogenous IDH1 mutation. R-2-HG influx into endothelial cells elevates the mobility of endothelial cells by regulating mitochondrial respiration.

R-2-HG hijacks SLC1A1 to promote mitochondrial Na$^+$/Ca^{2+} exchange and mitochondrial respiration in vascular endothelial cells

It remained unclear how mitochondrial respiration was activated by R-2-HG. R-2-HG can be converted to α-KG, an intermediate of TCA cycle, by D-2-hydroxyglutarate dehydrogenase (D2HGDH).[33] To test whether R-2-HG fuels TCA cycle via this mechanism, [U-^{13}C$_5$]-labeled R-2-HG was used as a tracer to measure its fractional contribution to ^{13}C-labeled TCA cycle-related metabolites, yet its contribution to α-KG and other mitochondria-related metabolites was neglectable (Supplementary information, Fig. S5a). These data largely excluded the possibility of active mitochondrial metabolism of R-2-HG in HUVECs. To better understand the kinetics of R-2-HG, R-2-HG levels in the supernatant or cell pellets in HUVECs culture were measured following pulse exposure to R-2-HG for 1 h. We observed a rapid decline of intracellular R-2-HG, along with an associated increase in the supernatant (Supplementary information, Fig. S5b). In contrast, prolonged treatment of R-2-HG could maintain the intracellular R-2-HG level (Supplementary
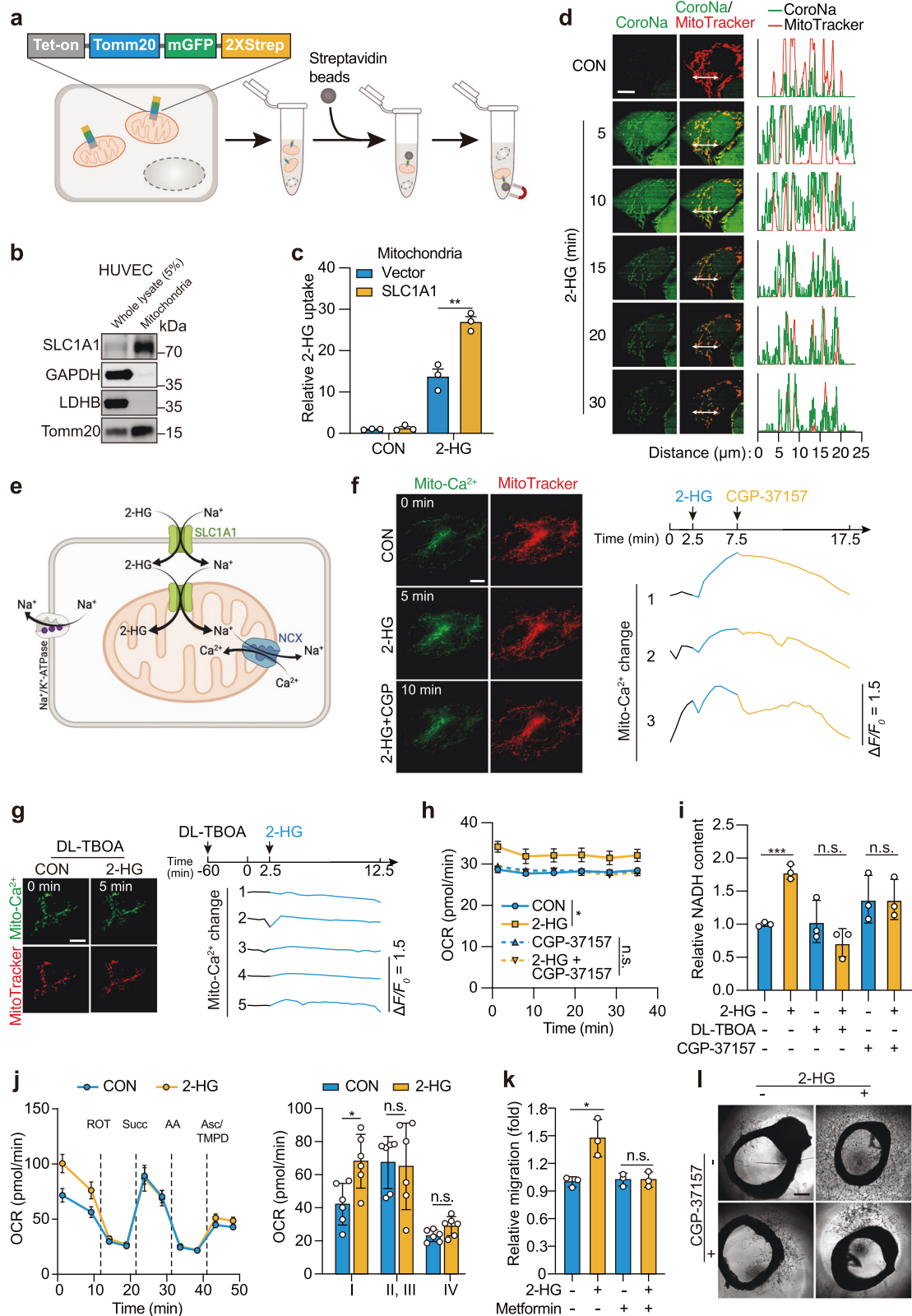
information, Fig. S5c). These results suggest a balanced influx/outflux cycle that allows for a dynamic equilibrium of intracellular R-2-HG.

Given that SLC1A1 is a glutamate carrier,[23] we asked whether the high concentration of extracellular R-2-HG may interfere the glutamate uptake and result in the compensatory mitochondrial activation. However, glutamate uptake was not affected by R-2-HG treatment, largely excluding this possibility as well (Supplementary information, Fig. S5d). Recently, it has been noted that SLC1A1-mediated glutamate transportation in mitochondria

Fig. 5 R-2-HG influx promotes mitochondrial Na$^+$/Ca^{2+} exchange in vascular endothelial cells. a Schematic diagram of mitochondria purification with Mito-2Strep. The expression of the fusion protein, Tomm20-mGFP-twin strep (Mito-2Strep), is controlled by a tetracycline-inducible promoter. **b** SLC1A1 expression in the purified mitochondria. HUVECs expressing Mito-2Strep were incubated with streptavidin magnetic beads for mitochondria purification. Purified mitochondria were subjected to immunoblotting. Tomm20, mitochondria marker; LDHB and GAPDH, cytosol markers. **c** The impact of SLC1A1 overexpression on mitochondrial R-2-HG uptake. Mitochondria purified as described in Supplementary information, Fig. S5f were exposed to R-2-HG (10 mM) for 1 h. **d** Time-lapse analysis of Na$^+$ influx in HUVECs. R-2-HG (10 mM) was added at 1 min. Shown were snapshots of fluorescence images (left) and representative traces (right) of Na$^+$ dynamics (green) and mitochondria pattern (red) along the double-headed white arrows indicated. Scale bar, 10 μm. **e** Schematic model of R-2-HG-induced mitochondrial Na$^+$/Ca^{2+} exchange. **f, g** Time-lapse analysis of mitochondrial Ca^{2+} influx. R-2-HG (10 mM), CGP-37157 (10 μM, **f**) and DL-TBOA (300 μM, **g**) were added at indicated time-points. Shown were snapshots of fluorescence images and representative traces of mitochondrial Ca^{2+} dynamics of HUVECs expressing 4mt-GCaMP6. Scale bar, 10 μm. **h** OCR measurement. HUVECs were treated with R-2-HG (10 mM) plus CGP-37157 (10 μM) for 1 h ($n = 4$). **i** NADH production. HUVECs were treated with R-2-HG (10 mM) plus CGP-37157 (10 μM) or DL-TBOA (300 μM) for 1 h. **j** OCR measurement for electron flow assay. Rotenone (ROT, 2 μM), succinate (Succ, 10 mM), antimycin A (AA, 4 μM) and ascorbate/tetramethyl-phenylenediamine (Asc/TMPD, 10 mM/100 μM) were added as indicated ($n = 6$). Quantification of individual mitochondrial complexes activity (right) was based on OCR measurement (left). **k** Transwell migration assay. HUVECs pre-treated with metformin (1 mM) for 1 h were exposed to R-2-HG (10 mM) for 24 h. Shown were quantification of the migration change. **l** Aortic ring sprouting assay. Matrigel-ring mixture was treated with R-2-HG (10 mM) plus CGP-37157 (10 μM) for 7 days. Scale bar, 500 μm. All the images were representative results from at least three independent experiments. All data represent means of indicated technical replicates; error bars represent SEM. Statistical analyses were performed using Student's t-test. ns, not significant. *$P < 0.05$, **$P < 0.01$, ***$P < 0.001$.

regulates the mitochondrial ATP synthesis via controlling Na$^+$/Ca^{2+} homeostasis in neurons and glial cells.[34,35] These findings inspired us to propose a possibility that SLC1A1-mediated R-2-HG influx may disturb mitochondrial Na$^+$/Ca^{2+} homeostasis and promote mitochondrial ATP production in endothelial cells. To test this possibility, we firstly examined the sub-cellular localization of SLC1A1. Visualization of SLC1A1-EGFP fusion protein in 293T cells indicated that, in addition to cell membrane, SLC1A1 was located in mitochondria (Supplementary information, Fig. S5e), consistent with previous studies.[35,36] The mitochondrial localization of SLC1A1 was further confirmed by an affinity mitochondria purification using a twin strep tag in both HUVEC and 293T cells[37] (Fig. 5a). In fact, SLC1A1 was found primarily enriched in the mitochondrial fraction (Fig. 5b; Supplementary information, Fig. S5f), suggesting a possibility of intracellular trafficking of R-2-HG from cytoplasm to mitochondria. To further test this possibility, purified mitochondria from 293T-SLC1A1 and the parental cells were exposed to R-2-HG, respectively. SLC1A1 expression resulted in the increased R-2-HG uptake in mitochondria (Fig. 5c).

We next examined whether SLC1A1-mediated R-2-HG influx may disturb mitochondrial Na$^+$ homeostasis. A time-lapse analysis of Na$^+$ dynamics showed that R-2-HG treatment caused a striking and instant surge of intracellular Na$^+$ signaling, followed by a rapid decline of the cytosolic Na$^+$ level, likely to preserve the Na$^+$ gradient across the plasma membrane by Na$^+$/K$^+$-ATPase.[38] Of note, the transient Na$^+$ influx shortly turned into a sustained mitochondrial Na$^+$ signal (Fig. 5d). Increased mitochondrial Na$^+$ gradient could activate the mitochondrial membrane Na$^+$/Ca^{2+} exchangers (NCXs),[39] among which NCX1 is ubiquitously expressed and could facilitate bidirectional ionic exchange.[40,41] We thus speculated that R-2-HG-caused mitochondrial Na$^+$ accumulation may induce Ca^{2+} influx, leading to subsequent bioenergetic alterations (Fig. 5e). In fact, R-2-HG treatment rapidly stimulated the mitochondrial Ca^{2+} influx (Fig. 5f; Supplementary information, Video S1), while the cytosolic Ca^{2+} signaling exhibited an opposite trend (Supplementary information, Fig. S5g). Pharmacological inhibition of NCXs using CGP-37157 reversed these changes (Fig. 5f; Supplementary information, Video S1 and Fig. S5g). Pre-inhibition of SLC1A1 prevented R-2-HG-induced mitochondrial Ca^{2+} signaling (Fig. 5g). These results proved a rapid mitochondrial Ca^{2+} influx resulted from Na$^+$/Ca^{2+} exchange, though we cannot rule out the impact of R-2-HG on the total intracellular Ca^{2+} level due to the lack of proper probes. To detect whether R-2-HG-triggered mitochondrial Ca^{2+} influx is only an acute metabolic change, we examined the mitochondria Ca^{2+} level upon a short (1 h) or long (24 h) treatment of R-2-HG, respectively. Mitochondrial Ca^{2+} signaling was sustained for 24 h

(Supplementary information, Fig. S5h), likely due to a persistent uptake of R-2-HG. Moreover, blockage of Na$^+$/Ca^{2+} exchange abrogated the impact of R-2-HG on the mitochondrial respiration (Fig. 5h), further confirming that R-2-HG-stimulated Na$^+$/Ca^{2+} exchange accounted for the mitochondrial activation.

Ca^{2+} signaling links to mitochondrial metabolism via activating a number of TCA dehydrogenases.[42] We discovered that NADH production in endothelial cells was significantly elevated by R-2-HG treatment in a time-dependent manner (Supplementary information, Fig. S5i), and this change could be abolished by the inhibition of either SLC1A1 or NCXs (Fig. 5i), suggesting a Na$^+$/Ca^{2+} exchange-dependent NADH production stimulated by R-2-HG influx. NADH fuels the mitochondrial complex I to promote ATP synthesis.[42] Consistently, analysis of individual mitochondrial complexes upon R-2-HG treatment revealed that R-2-HG specifically activated the complex I rather than other complexes (Fig. 5j; Supplementary information, Fig. S5j). Inhibition of mitochondrial complex I using metformin attenuated R-2-HG-provoked HUVEC migration (Fig. 5k; Supplementary information, Fig. S5k). These results demonstrated that Ca^{2+} influx and the associated activation of mitochondrial complex I accounted for R-2-HG-elevated mitochondrial respiration. In line with these results, inhibition of NCXs eliminated the impact of R-2-HG on HUVEC migration (Supplementary information, Fig. S5l) and aortic ring sprouting (Fig. 5l). Together, we discovered that R-2-HG hijacks SLC1A1 to promote mitochondrial Na$^+$/Ca^{2+} exchange to fuel mitochondrial respiration.

Mitochondrial respiration fuels cytoskeleton rearrangement and mitochondrial migration
We next investigated how mitochondrial respiration empowered cell migration. The switch of endothelial cells from quiescence to migratory status requires the rapid production of ATP,[43] and mitochondria is the powerhouse of ATP production. We hence examined the dynamics of mitochondrial Ca^{2+} influx and ATP levels upon R-2-HG treatment. A time-lapse analysis showed that the rapid mitochondrial Ca^{2+} influx was associated with an increase in mitochondrial ATP production (Fig. 6a; Supplementary information, Video S2), and the latter could be impeded by the inhibition of NCXs (Supplementary information, Fig. S6a and Video S3) or SLC1A1 (Supplementary information, Fig. S6b), suggesting that R-2-HG treatment promotes ATP generation via promoting Na$^+$/Ca^{2+} exchange. These results were confirmed by Seahorse analysis (Supplementary information, Fig. S6c).

ATP hydrolysis is required for the remodeling of the actin cytoskeleton to enable cell mobility change.[44] We hence examined the impact of R-2-HG on cytoskeleton. R-2-HG
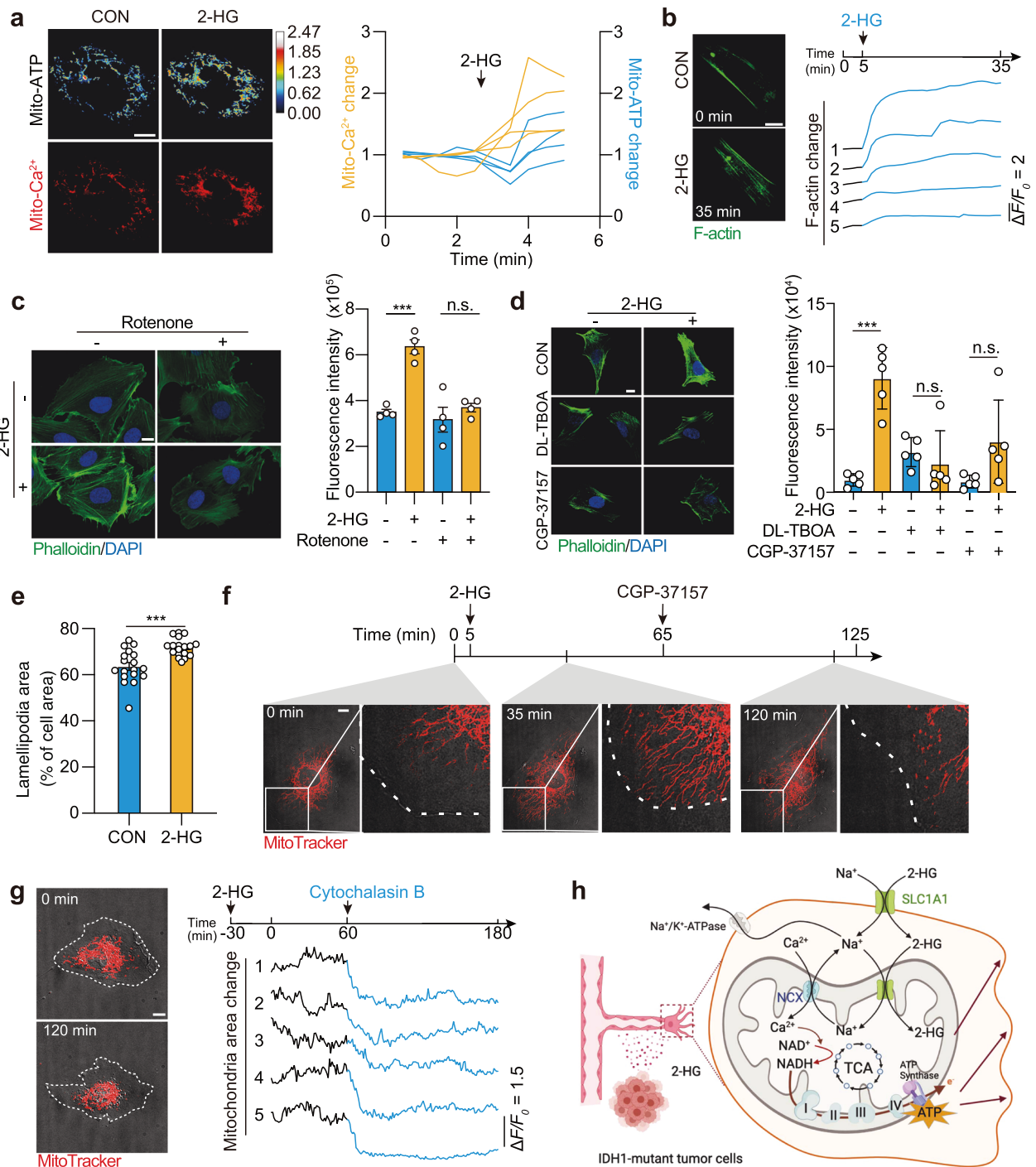
Fig. 6 R-2-HG remodels cytoskeleton rearrangement and promotes mitochondrial migration. a R-2-HG-induced mitochondrial Ca^{2+} signaling and ATP production. HUVECs expressing 4mt-ATeam1.03 were pre-incubated with Rhod-2 (2.5 μM) for 30 min and treated with R-2-HG (10 mM) at 2.5 min. Left, snapshot of pseudocoloured and fluorescence images of time-lapse videos. Pseudocolour bars indicate the YFP/CFP emission ratio. Right, representative traces of mitochondrial Ca^{2+} (Rhod-2) and mitochondrial ATP (4mt-ATeam1.03) dynamics. **b** R-2-HG-induced F-actin formation. HUVECs were pre-incubated with CellMask Green Actin Tracking Stain for 30 min. R-2-HG (10 mM) was treated at 5 min. Left, snapshot of fluorescence images of time-lapse videos. Right, representative traces of F-actin formation dynamics. **c**, **d** The impact of the mitochondrial respiration, Na^+/Ca^{2+} exchange and R-2-HG uptake on F-actin formation. HUVECs were treated with R-2-HG (10 mM) alone or in combination with rotenone (2 μM, **c**), DL-TBOA (300 μM, **d**) or CGP-37157 (10 μM, **d**) for 1 h. F-actin was probed with AlexaFluor 488-phalloidin and quantified by fluorescence intensity. **e** Quantification of the lamellipodia area upon R-2-HG treatment. HUVECs were treated with R-2-HG (10 mM) for 30 min. **f** R-2-HG-induced mitochondrial migration in HUVECs. Cells were treated with R-2-HG (10 mM) and CGP-37157 (10 μM) at the indicated time-points. Mitochondria were visualized by MitoTracker Red. Shown were snapshots of fluorescence images of time-lapse videos of mitochondrial redistribution. **g** Cellular distribution of mitochondria. HUVECs were treated with R-2-HG (10 mM) for 1 h followed by cytochalasin B (1 μM) for 2 h. Mitochondria were visualized as assay in **f**. **h** Schematic model showing the mechanism of R-2-HG-mediated tumor-endothelial cell interplay in tumor angiogenesis. All the images show representative results from at least three independent experiments. Scale bar, 10 μm. For all bar graphs, data represent means of indicated technical replicates; error bars represent SEM. Statistical analyses were performed using Student's t-test. ns, not significant. ***$P < 0.001$.
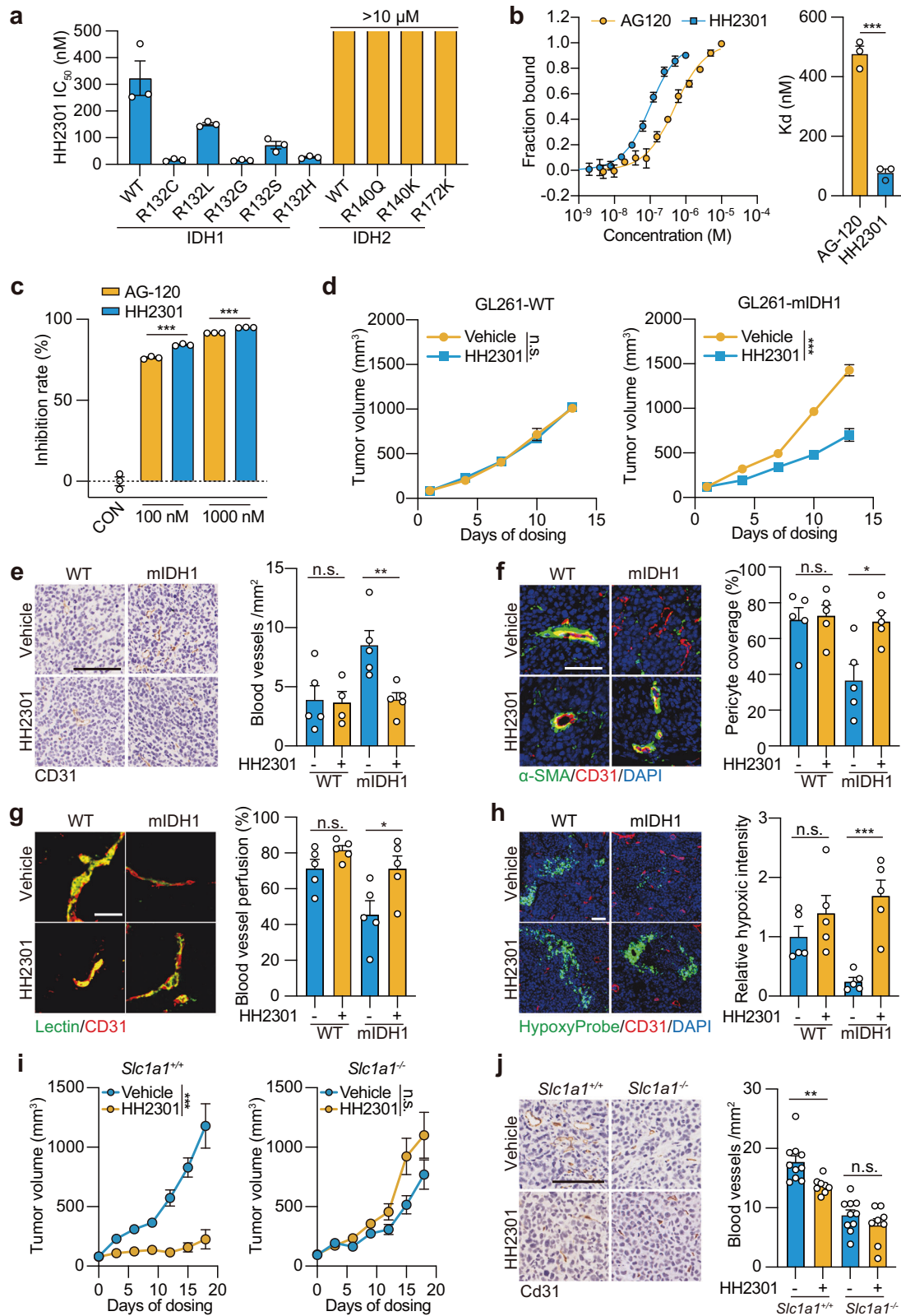
treatment rapidly stimulated the formation of actin filaments (F-actin) in HUVECs (Fig. 6b), which was largely blocked by the inhibition of mitochondrial complex I (Fig. 6c; Supplementary information, Fig. S6d), ATP synthase (Supplementary information, Fig. S6e), SLC1A1, or Na^+/Ca^{2+} exchangers (Fig. 6d). These results

imply that R-2-HG-stimulated cytoskeleton rearrangement requires Na^+ influx and the associated Na^+/Ca^{2+} exchange.

Migrating endothelial cells are generally believed to rely on glycolysis for rapid ATP production, supported by the redistribution of glycolytic enzymes at the lamellipodia for local ATP

Fig. 7 mIDH inhibition suppresses tumor angiogenesis in IDH1-mutant tumors. a IC_{50} of HH2301 towards wild-type IDH1/2 or different mutant forms. **b** Kd values of AG-120 and HH2301 binding to recombinant IDH1-R132C protein. Kd values were determined using MST assay. Left, Kd fitting curves of AG-120 and HH2301 binding to IDH1-R132C protein. Right, Kd values calculated from Kd fitting curves. **c** Inhibition of R-2-HG accumulation in the supernatant. ICC302 cells were treated with AG-120 and HH2301 at indicated concentrations for 48 h. **d** Tumor growth curve. GL261-WT and -mIDH1 cells were inoculated into nude mice ($n = 5$) and tumor-bearing mice were treated with HH2301 (300 mg/kg, gavage, twice per day) or vehicle control. **e** Blood vessel density in tumor tissues. Tumor tissues from assay shown in **d** were subjected to immunohistochemistry analysis for CD31 staining. Shown were representative images and quantification of CD31 staining. Scale bar, 100 μm. **f** Staining of pericyte coverage in tumor vasculature. Tumor tissues from assay shown in **d** were subjected to immunofluorescence staining using anti-α-SMA (green) and anti-CD31 (red) antibodies. Shown were representative images and quantification of α-SMA-positive vessels in total vessels. Scale bar, 50 μm. **g** Tumor vascular perfusion. Mice used in **d** were intravenously injected with FITC-lectin (green) before tumors were collected. Tumor blood vessels were revealed by CD31 staining (red). Shown were representative images and quantification of lectin-positive vessels in total vessels. Scale bar, 50 μm. **h** Tumor hypoxia analysis. Mice used in **d** were intravenously injected with pimonidazole hydrochloride before tumors were collected. Tumor tissues were subjected to immunofluorescence staining using Hypoxyprobe-1-Mab1 FITC (green) and anti-CD31 (red) antibodies. Scale bar, 50 μm. **i** Tumor growth curve. GL261-mIDH1 cells were inoculated into wild-type (SLC1A1$^{+/+}$) or SLC1A1$^{-/-}$ C57BL/6 mice ($n \geq 8$). Mice were treated with HH2301 (300 mg/kg, gavage, twice per day) or vehicle control for indicated days. **j** Blood vessel density in tumor tissues from assay shown in **i**. Scale bar, 100 μm. For all graphs, data in **b** and **c** are means of indicated technical replicates and data in **d**–**j** represent means of individual mice; error bars represent SEM. Statistical analyses were performed using Student's t-test. ns, not significant. $*P < 0.05$, $**P < 0.01$, $***P < 0.001$.

supply.[45] We thus asked whether mitochondria could redistribute upon R-2-HG treatment. A time-lapse analysis of subcellular distribution of mitochondria in HUVECs showed that along with larger and front-to-back distributed lamellipodia projection areas (Fig. 6e), mitochondria moved to the leading front of lamellipodia in HUVECs upon R-2-HG treatment (Fig. 6f; Supplementary information, Video S4). These results suggest that the redistributed mitochondria might act as a local ATP supplier for the cell migration. Of note, cytoskeleton is required to direct mitochondria movement.[46] When disrupting F-actin formation by cytochalasin B, R-2-HG-caused mitochondrial redistribution was impeded as well (Fig. 6g). These data suggest that mitochondrial respiration-facilitated cytoskeleton rearrangement promotes the mitochondrial redistribution for local ATP supply, which further supports the cytoskeletal rearrangement, indicating a positive feedback loop between mitochondrial migration and cytoskeletal rearrangement triggered by R-2-HG treatment.

Taken together, our findings identified SLC1A1-mediated mitochondrial R-2-HG influx and secondary mitochondrial Na$^+$/ Ca^{2+} exchange as a mechanistic link between IDH1-mutant cancer cells and surrounding endothelial cells (Fig. 6h). This finding suggests a new model showing how the physiological function of metabolite transporters is hijacked by oncometabolite R-2-HG to confer a survival benefit for tumor cells.

Pharmacological disruption of tumor–endothelial cell crosstalk inhibits tumor angiogenesis in IDH1-mutant tumors

Finally, we explored the therapeutic relevance of these mechanistic findings. Oncometabolite R-2-HG is involved in tumorigenesis in a variety of tissue types. However, the therapeutic benefit of mIDH1 inhibitors is limited to hematological tumors. A long-standing puzzle in mIDH1-targeted therapy is that R-2-HG depletion appears insufficient to inhibit the growth of IDH1-mutant solid cancer cells.[6,7] We asked whether disrupting tumor–endothelial cell crosstalk could possibly potentiate the anticancer activity of mIDH1 inhibition in solid tumors.

To probe this possibility, we employed the clinically approved mIDH1 inhibitor AG-120 and a new rationally designed mIDH1 inhibitor,[47] designated as HH2301 (Supplementary information, Fig. S7a). HH2301 is a potent and selective mIDH1 inhibitor (Fig. 7a). Compared with AG-120, HH2301 exhibited the superior activity towards different mutant forms of IDH1 except IDH1-R132H that is prevalent in LGG (Supplementary information, Fig. S7b). The superior potency of HH2301 compared with AG-120 might result from the improved binding affinity, as indicated by Kd values towards IDH1-R132C (Fig. 7b). Consistently, HH2301 exhibited the superior potency in diminishing R-2-HG production

in ICC302 and HT1080 cells bearing IDH1-R132C mutation (Fig. 7c; Supplementary information, Fig. S7c).

We next tested whether disrupting R-2-HG-mediated tumor–endothelial cell crosstalk could strengthen the anticancer activity of mIDH1 inhibitors in IDH1-mutant solid tumors. Consistent with previous reports,[48] both HH2301 and AG-120, even at concentrations up to 10 μM, barely affected the growth of a set of ICC cells (ICC302, HCCC9810 and RBE) similarly bearing IDH1 mutation or the glioma cell pair GL261-WT and -mIDH1 (Supplementary information, Fig. S7d). In contrast, in a co-culture composed of ICC302 cells and HUVECs, both compounds inhibited the migration (Supplementary information, Fig. S7e) and lumen-forming ability (Supplementary information, Fig. S7f) of endothelial cells promoted by IDH1-mutant tumor cells.

We further attempted to establish linkage between antitumor efficacy and angiogenesis change in vivo. In nude mice bearing GL261-WT or GL261-mIDH1 tumors, pharmacological inhibition of mIDH1 using HH2301 inhibited tumor growth of IDH1-mutant tumors without affecting the wild-type counterpart (Fig. 7d). Consistent with the tumor growth change, the tumor blood vessel density (Fig. 7e) in the mutant tumors was decreased to a level comparable to the wild-type tumors by HH2301 treatment. Further assessment of tumor vasculature, blood vessel perfusion and tumor hypoxia confirmed the linkage between mIDH1 inhibition and tumor angiogenesis. Specifically, mIDH1 inhibition relieved the abnormality of tumor vasculature (Fig. 7f; Supplementary information, Fig. S7g) and rescued the impaired vascular perfusion (Fig. 7g) in IDH1-mutant tumors, both of which were recovered to the level of wild-type tumors. Consistent with data shown above (Fig. 3i), tumor hypoxia in IDH1-mutant tumors was increased upon mIDH1 inhibition (Fig. 7h), which is likely due to the significant reduction of blood vessel numbers and tumor blood flow. These data suggest that pharmacological inhibition of mIDH1 suppresses angiogenesis in IDH1-mutant tumors. In support of these findings, mIDH1 inhibition in IDH1-mutant tumors did not affect tumor proliferation, as indicated by Ki67 staining (Supplementary information, Fig. S7h), but induced tumor cell death instead (Supplementary information, Fig. S7i), echoing the phenotype of angiogenesis inhibition in tumor tissues.[49]

Further, GL261-mIDH1 cells were implanted into wild-type or SLC1A1 knockout mice in parallel. The therapeutic effect of HH2301 in controlling tumor growth (Fig. 7i) and inhibiting tumor angiogenesis (Fig. 7j) was largely abolished in SLC1A1 knockout mice, further strengthening the role of disrupting R-2-HG-mediated tumor–endothelial cell crosstalk in conferring the antitumor effect of mIDH1 inhibitors.
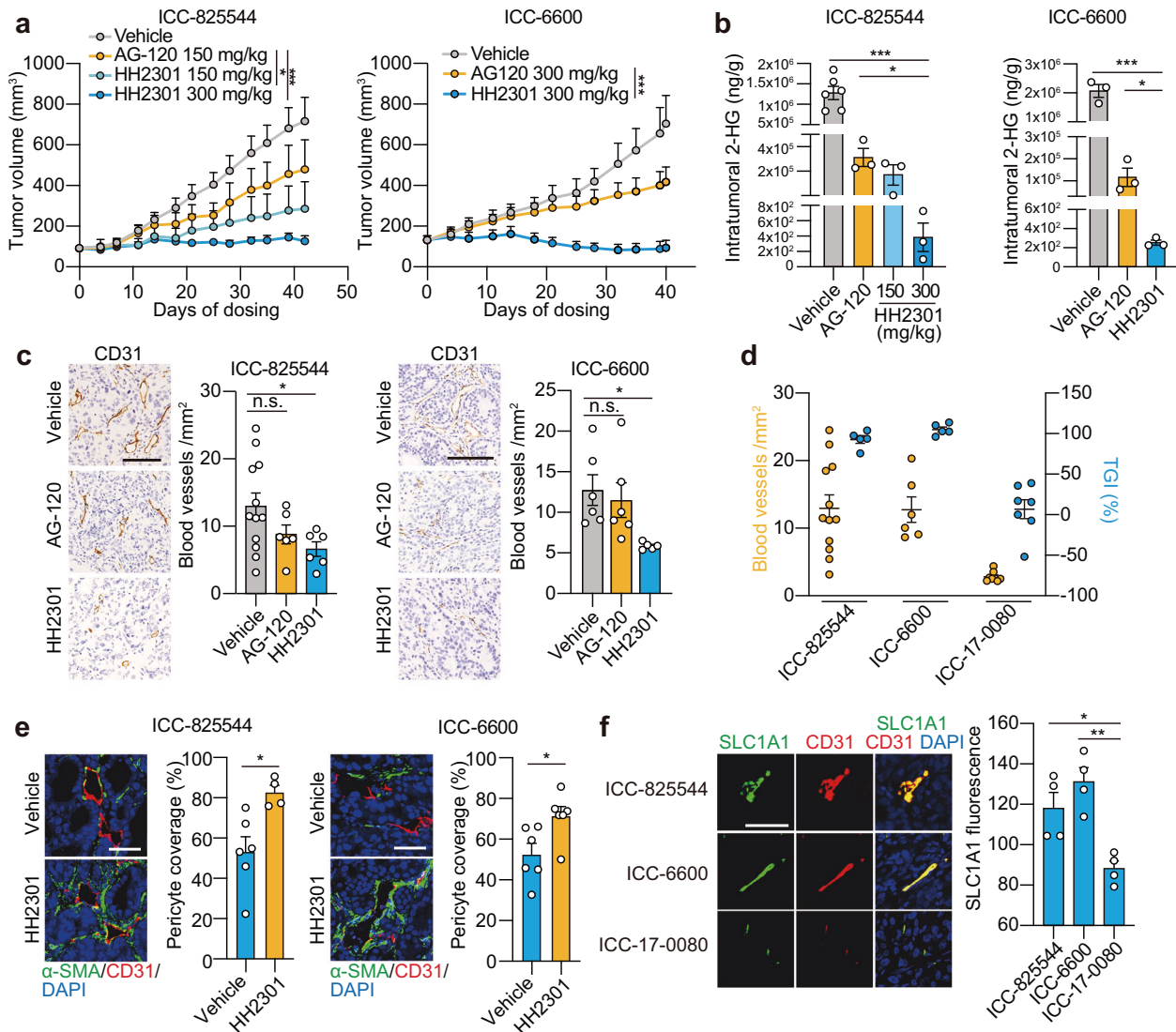
Fig. 8 Anticancer activity of mIDH1 inhibitors in IDH1-mutant cholangiocarcinoma. a Tumor growth of two cholangiocarcinoma PDX models bearing IDH1-R132C mutation. Tumor-bearing mice were treated with AG-120 or HH2301 at indicated doses (gavage, twice per day, $n \geq 5$). **b** Intratumoral R-2-HG amount. Tumor tissues from **a** were collected at the end of the study for R-2-HG analysis. **c** Tumor blood vessel density. Tumor tissues from **a** were subjected to CD31 immunohistochemical staining. Tumors treated with the same dose of HH2301 and AG-120 were selected for analysis (150 mg/kg for ICC-825544 model and 300 mg/kg for ICC-6600 model). Shown were representative images and quantification of CD31 staining. Scale bar, 100 μm. **d** Correlation between the basal intratumoral blood vessel density and the efficacy of HH2301 (300 mg/kg treatment group) in cholangiocarcinoma PDX models. ICC-825544 and ICC-6600 models were as described in **a**. ICC-17-008 is an IDH1-R132C mutant cholangiocarcinoma PDX model nonresponsive to HH2301 (See Supplementary information, Fig. S8e, f). TGI, tumor growth inhibition rate. **e** Staining of pericyte coverage in tumor vasculature. Tumor tissues as described in **d** were subjected to immunofluorescence staining using anti-α-SMA (green) and anti-CD31 (red) antibodies. Shown were representative images and quantification of α-SMA-positive vessels in total vessels. Scale bar, 50 μm. **f** SLC1A1 expression in IDH1-R132C mutant cholangiocarcinoma PDX models. Intrinsic SLC1A1 and CD31 expression levels in tumor sections were examined using RNA FISH analysis and quantified by measuring fluorescence intensity. Scale bar, 50 μm. Sample sizes were variable between assays as some tumors collected at the end of study were not sufficient to support all the analysis. All data represent means of individual mice; error bars represent SEM. Statistical analyses were performed using Student's t-test for **a** and **e**, and using one-way ANOVA for **a–c** and **f**. ns, not significant. *$P < 0.05$, **$P < 0.01$, ***$P < 0.001$.

mIDH1 inhibitors are potential treatment for IDH1-mutant cholangiocarcinoma

Cholangiocarcinoma, in particular intra-hepatic cholangiocarcinoma (ICC), is a highly heterogeneous disease with poor prognosis and currently lacks effective therapies. A recently completed clinical study has shown the promise of AG-120 in treating IDH1-mutant advanced cholangiocarcinoma patients, yet with relatively modest therapeutic benefit.[10] By analyzing IDH1 mutation status in ICC, we noticed that IDH1-R132C is the predominant mutant form among all the IDH1 mutation types (Supplementary information, Fig. S8a). Given the apparent advantage of HH2301

towards IDH1-R132C compared with AG-120 (Fig. 7b; Supplementary information, Fig. S7b), we further explored the therapeutic potential of HH2301 for this mutant type. Despite the marginal in vitro anticancer effect on cholangiocarcinoma LICCF-mIDH1 (R132C) cells, HH2301 significantly inhibited the tumor growth of LICCF-mIDH1 xenograft, associated with the suppressed tumor angiogenesis (Supplementary information, Fig. S8b–d).

Further, the anticancer efficacy of HH2301 was assessed in three cholangiocarcinoma PDX models, ICC-825544, ICC-6600 and ICC-17-0080, similarly bearing IDH1-R132C mutation. AG-120 was used as a control. HH2301 exhibited a significantly improved anticancer

activity compared with AG-120 in ICC-825544 and ICC-6600 models (Fig. 8a), which was associated with the diminished R-2-HG production in tumor tissues (Fig. 8b). However, neither compound was able to control the tumor growth in ICC-17-0080 model (Supplementary information, Fig. S8e), despite the remarkably diminished R-2-HG production (Supplementary information, Fig. S8f). We asked whether the differential therapeutic response is due to the impact on tumor angiogenesis. Intratumoral CD31 staining revealed the inverse correlation of reduced blood vessel intensity and tumor growth in ICC-825544 and ICC-6600 models, both showing relatively higher level of tumor blood vessel density (Fig. 8c, d). In contrast, ICC-17-0080 model that was non-responsive to HH2301, exhibited a lower basal level of blood vessel density in tumor tissues (Fig. 8d). These results suggest that the restrained tumor angiogenesis may confer in vivo efficacy of mIDH1 inhibition. Consistently, mIDH1 inhibition by HH2301 normalized tumor vasculature, indicated by the improved pericyte and collagen coverage in ICC-825544 and ICC-6600 tumors (Fig. 8e; Supplementary information, Fig. S8g), while abnormal vasculature was barely affected by HH2301 treatment for ICC-17-0080 tumors (Supplementary information, Fig. S8h). Moreover, the differential impact of HH2301 in the three PDX models was associated with SLC1A1 expression in endothelial cells (Fig. 8f). This may explain the lack of response to mIDH1 inhibition in ICC-17-0080 model.

Our findings suggest that disruption of R-2-HG-promoted tumor angiogenesis may largely contribute to the tumor growth inhibition by mIDH1 inhibitors. These insights were consistent with previous notion that tumor-associated angiogenesis is associated with the poor prognosis of cholangiocarcinoma,[50] though ICC is believed to be hypovascular in the tumor microenvironment.[51] For further confirmation, we also analyzed two reported ICC cases, both of which gained IDH1 mutation during tumor recurrence.[52] The levels of CD31 and CD34, two vascular markers, were both upregulated in the recurrent tumor tissues compared with the primary tumors (Supplementary information, Fig. S8i). Our results together suggest that blockage of tumor–endothelial cell crosstalk contributes to the anticancer activity of mIDH1 inhibitors in treating cholangiocarcinoma.

DISCUSSION

Gain-of-function hotspot mutations in IDH1 are among the most common genetic lesions in ICC that feature complicated tumor microenvironments and heterogenicity. However, in vitro studies using ICC cells did not observe the therapeutic effect of mIDH inhibitors[48] and in vivo studies applying mIDH1 inhibitors in ICC animal models is lacking. The recently completed clinical study of AG-120 in ICC patients obtained modest therapeutic benefit, in which most responsive patients exhibited stable disease.[10] This therapeutic outcome is believed to reflect a presumed mechanism related to the reversed epigenetic modifications and the differentiation of liver progenitor cells.[10,53–56] In this study, we provide the first evidence showing that IDH1-mutant cholangio-carcinoma PDX models are responsive to mIDH1 inhibitors, yet quantitative proteomic analysis of tumor tissues did not show significant change in protein levels of hepatocyte and biliary markers upon the treatment (Supplementary information, Fig. S8j). Instead, we discovered that the disruption of R-2-HG-promoted tumor angiogenesis may account for, at least partially, the efficacy of mIDH1 inhibitors in treating IDH1-mutant cholangiocarcinoma. The expression of SLC1A1 in vascular endothelial cells is required for R-2-HG-mediated crosstalk between tumor and endothelial cells, and is associated with the anticancer activity of mIDH1 inhibitors in cholangiocarcinoma PDX models. These results provide important insights for understanding the therapeutic implications of mIDH1 inhibitors in treating solid tumors.

Different from tumor cells that produce massive endogenous R-2-HG, the uptake of R-2-HG by environmental non-tumor cells could be limited by the efficiency of transporters, resulting in disadvantages in competing with α-KG. In this study, we show that R-2-HG treatment at a pathologically-relevant concentration results in about 20-fold of intracellular R-2-HG/α-KG ratio, much lower than that caused by the treatment of Octyl-R-2-HG, a cell membrane permeable R-2-HG derivative, with even lower doses, and in turn is insufficient to inhibit α-KG-dependent histone demethylases (Fig. 4b, c). This observation is consistent with a previous report showing that R-2-HG competition with α-KG for dioxygenases requires a concentration at least 500-fold higher than that of α-KG.[13] This finding provides an explanation for the divergent mechanisms of R-2-HG in non-tumor cells. For example, it has been lately revealed that R-2-HG uptake suppresses T cell immunity without causing the reprogramming of epigenome.[16] Likewise, R-2-HG in macrophages of IDH1-mutant glioma re-orchestrates tryptophan metabolism and drives immunosuppressive myeloid states independent of epigenome change.[15] In this study, we also discover a new mechanism that SLC1A1-mediated mitochondrial influx of R-2-HG promotes Ca^{2+} influx and activates mitochondrial respiration in endothelial cells. Moreover, it might be worth mentioning that quite a few studies used Octyl-R-2-HG to facilitate R-2-HG uptake in cell-based studies, yet this approach might not correctly simulate the pathological condition, in particular for non-tumor cells. In fact, previous studies that are able to observe the epigenome changes upon extracellular R-2-HG treatment all used Octyl-R-2-HG,[13,32,57–60] while those using R-2-HG treatment did not observe the impact on epigenome[16] or HIF-1α.[61] These insights may suggest new directions for understanding the role of R-2-HG in the tumor microenvironment.

As most of the metabolites are cell membrane impermeable and require specialized membrane proteins to facilitate their transmembrane transport, metabolite transporters are gatekeepers to regulate the metabolic crosstalk between different cells. In this study, we discover a novel role of SLC1A1 in specifically orchestrating the metabolic crosstalk between IDH1-mutant tumor cells and vascular endothelial cells via transporting extracellular R-2-HG into endothelial cells. The interaction between R-2-HG and SLC1A1 is likely due to the structural similarity between R-2-HG and glutamate or aspartate, the reported substrates of SLC1A1.[62] Apart from SLC1A1, SLC13A3, SLC22A6 and SLC22A11 have all been reported as R-2-HG transporters, though functioning in different cell context, including T cells,[16] kidney cells and astrocytes.[63] According to our results, these transporters are at an extremely low level in endothelial cells, and we identify SLC1A1 as a new transporter for R-2-HG uptake in endothelial cells. The cell type- and organelle-dependent expression of metabolic transporters may partially explain the heterogenous impact of R-2-HG in the tumor microenvironment. For example, R-2-HG has been reported to suppress mitochondrial respiration in T cells[16] via inhibiting ATP synthase, while a recent study reveals that R-2-HG barely affects mitochondrial respiration in leukemia cell lines[32] and our study demonstrates R-2-HG promotes mitochondrial respiration in endothelial cells. Moreover, we also show that SLC1A1 is unlikely to be involved in R-2-HG export (Supplementary information, Fig. S2h). SLC1A1 is barely expressed in tumor cells, including IDH1-mutant tumors known for active R-2-HG export (Supplementary information, Fig. S2e), suggesting other transporters being responsible for releasing R-2-HG from tumors. Previous studies have reported that SLC22A11 mediates the secretion of intracellular 2-HG in renal cells.[63] Whether other transporters are involved in R-2-HG export in IDH1-mutant tumors remains to be investigated.

Other host cells in the tumor microenvironment, including immune cells and fibroblasts, are all able to take up R-2-HG, though relatively at a less extent (Fig. 1d). It has been reported that tumor-derived R-2-HG could modulate the function of T cells and macrophages to inhibit antitumor immunity,[15,16] yet its

impact on fibroblasts is unknown. In our study, we show that R-2-HG confers tumor growth advantage and antitumor efficacy of mIDH1 inhibition independent of regulating immunity by using immune-deficient nude mice. Meanwhile, it is also noted that the difference in tumor growth between IDH1-WT and mIDH1 tumors (Fig. 1k) and the antitumor efficacy of mIDH1 inhibitor (Fig. 7d) in immune-deficient nude mice are both less striking compared with those in immune-competent C57BL/6 mice (Fig. 7i; Supplementary information, Fig. S1l), suggesting that the impaired antitumor immunity and the enhanced angiogenesis together contribute to the pro-tumor effect of R-2-HG. Interestingly, in immune-competent SLC1A1$^{-/-}$ mice where the pro-angiogenesis of R-2-HG was diminished, the therapeutic effect of mIDH1 inhibition was completely abolished as well (Fig. 7i). This may be attributed to the irreversible T cell exhaustion induced by longer-exposure to R-2-HG in SLC1A1-deficient mice due to slower tumor growth. Another possibility is that SLC1A1 might be involved in the regulation of immunity in IDH1-mutant tumors, which remains to be further investigated.

Together, our findings make contributions to the field in four aspects. (1) We identify SLC1A1 as a new transporter of R-2-HG uptake. (2) We reveal a new working model showing how oncometabolites hijack metabolite transporters to remodel the tumor microenvironment and confer a survival benefit for tumor cells. (3) We provide explanations for the increasingly noted divergent mechanisms of R-2-HG in different cell context, which may potentially extend to other metabolites. (4) Our mechanistic insights point to a new direction to understand the therapeutic benefit of mIDH1 inhibitors in treating IDH1-mutant solid tumors, in particular cholangiocarcinoma.

Our study has a few limitations. For example, we used SLC1A1 full-knockout mice to demonstrate its role in vascular endothelial cells, as SLC1A1 is specifically expressed in vascular endothelial cells in the tumor microenvironment (Fig. 2c; Supplementary information, Fig. S2e). Our findings could be further strengthened using endothelial-specific knockout of SLC1A1. Moreover, our results based on in vitro assays using primary vascular endothelial cells show that R-2-HG promotes mitochondrial respiration to fuel endothelial cell migration, but not proliferation, suggesting a phenotype driven by endothelial tip cell alteration. Due to the technical limitations, these findings cannot be further confirmed in vivo at this stage.

MATERIALS AND METHODS
Animal studies
SLC1A1$^{-/-}$ mice were generated by Shanghai Model Organisms Center. C57BL/6 mice and BALB/c nude mice of 6–8 weeks old (female) were obtained from Shanghai Lingchang Biotechnology and randomly assigned to experimental groups. Animal studies were performed under the approval of the Institutional Animal Care and Use Committee at Shanghai Institute of Materia Medica, Chinese Academy of Sciences. The studies of cholangiocarcinoma PDX models were approved and performed according to the IACUC at WuXi AppTec, CrownBio and Shanghai Institute of Materia Medica, Chinese Academy of Sciences. During all the studies, the care and use of animals were conducted in accordance with the regulations of the Association for Assessment and Accreditation of Laboratory Animal Care (AAALAC). TGI rate was measured using the formula: TGI (%) = [1 − (V$_t$ − V$_0$ in treated group)/(V$_t$ − V$_0$ in control group)] × 100, where V$_t$ is the tumor volume on the indicated day of dosing and V$_0$ is the tumor volume at the beginning of the treatment. HH2301 was provided by Haihe Biopharma (Shanghai, China) and AG-120 (#MB3230) was purchased from Dalian Meilun Biotechnology Corporation (Dalian, China).

Cell culture
HT1080, HEPG2, PC3, A549, CACO2, HELA, T47D, JURKAT, MCF7, U937, THP-1, RPMI8226, SKBR3, RH30, HEK293 and 293T cells were purchased from American Type Culture Collection (ATCC, Manassas, USA). Glioma 261, HCCC9810 and RAW264.7 cells were purchased from Nanjing COBIOER

Biotechnology Co., Ltd (Nanjing, China). ICC302 and RBE cells were from Zhongshan Hospital (Shanghai, China). DAUDI, K562 and HL60 cells were purchased from Type Culture Collection of Chinese Academy of Sciences. GM00637 cells were purchased from Coriell Institute (Camden, NJ, USA). Primary HUVECs were purchased from ScienCell Research Laboratories (Carlsbad, CA, USA). Primary HRECs were from Shanghai University of Traditional Chinese Medicine. LICCF cells were from Eastern Hepatobiliary Surgery Institute, Second Military Medical University (Shanghai, China). All cells were cultured and processed as suppliers suggested. Primary cells used in this study were within 3 to 6 passages. The identity of cell lines was routinely confirmed using short tandem repeat analysis at Genesky Biotechnologies (Shanghai, China).

Proliferation assay
Cells were plated at an appropriate density in 96-well plates and incubated for overnight, then treated as indicated for 72 h. Cell proliferation was assessed by the sulforhodamine B (SRB) staining using a SpectraMax PLUS384 microplate reader (Molecular Device, USA) at 560 nm, or monitored by the live-cell analysis system IncuCyte® (Essen BioScience Ltd., Hertfordshire, UK). Growth curves were plotted with the confluence percentage.

Metabolic flux analysis
In [U-^{13}C$_5$]-labeled R-2-HG tracer experiments, cells were cultured in DMEM medium (#D5030, Sigma-Aldrich) supplied with 10 mM glucose, 1 mM pyruvate and 2 mM glutamate, followed by the treatment with [U-^{13}C$_5$]-labeled R-2-HG (3 mM) (#36106, Sigma-Aldrich).

For the competitive uptake of R-2-HG and glutamate, cells were cultured in DMEM medium (#D5030, Sigma-Aldrich) supplied with 10 mM glucose and 1 mM pyruvate, followed by the treatment with [U-^{13}C$_5$]-labeled glutamate (2 mM) (#CLM-3949, Cambridge Isotope Laboratories) and R-2-HG (10 mM) (#S137414, Aladdin) for 6 h.

In the analysis of glutamate uptake, cells transfected with indicated plasmids were pre-cultured in DMEM medium (#D5030, Sigma-Aldrich) supplied with 10 mM glucose and 1 mM pyruvate for 2 h, followed by the treatment of [U-^{13}C$_5$]-labeled glutamate (100 μM) for 0.5 h.

^{13}C-incorporated metabolites were analyzed by GC-MS and normalized by cell numbers. Sample preparation, derivatization and instrumental analysis were performed as described before.[64]

Metabolome analysis
For non-targeted metabolomic analysis, cell samples were derivatized and injected into GC-MS instrument in 1 μL volume. Samples were separated in helium as carrier gas at a flow rate of 1 mL/min and the temperature of injection and transfer interface was set to 270 °C. The measurements were made using electron impact ionization in the full scan mode. A time-of-flight mass spectrometry (GC-TOF/MS) system (Pegasus HT, Leco, MO, USA) with an Agilent 7890B gas chromatography and a Gerstel multipurpose sample MPS2 with dual heads (Gerstel, Muchlheim, Germany) were used for metabolomic analysis. A Rxi-5 ms capillary column (Restek, Bellefonte, USA) was used for separation.

Among 138 metabolites identified by non-targeted metabolomic analysis, 15 metabolites were found increased upon R-2-HG treatment with a cutoff of fold change > 1.2. Enrichment analysis was performed on these metabolites using the web tool MetaboAnalyst with Small Molecule Pathway Database (SMPDB) as metabolite set library.

R-2-HG measurement
For the measurement of R-2-HG, 100 mg tumor tissues were homogenated in 1 mL PBS, followed by an ultrasonic treatment for 15 min in ice-cold water. Cells were washed three times by PBS and collected using cell scrapers. To extract R-2-HG, PBS was removed and cells were lysed in 200 μL ice acetonitrile solution of S-2-HG-D5, a Deuterium-labeled analog of S-2-HG serving as an internal standard, at −80 °C for 30 min. Pyridine buffer was prepared by combining 1.8 mL of HCl (12 M), 2.87 mL of pyridine and 28.7 mL of water (pH around 5.0). 25 μL of the standard solution or test samples were mixed with 50 μL of 1 M O-Benzylhydroxylamine (Sigma, B-22984-5g) and 50 μL of 1 M 3-(ethyliminomethylideneamino)-N,N-dimethylpropan-1-amine (Sigma, 39391-10 mL) in the pyridine buffer. After 30 min at room temperature, 300 μL of ethyl acetate was added and the plates were shaken for 20 min followed by centrifugation for 5 min at 1900 rpm, and then 50 μL of organic layer was taken into a 96-well plate. The aqueous layer was dried

using a stream of nitrogen at 40 °C and reconstituted in 300 μL of methanol/water (50: 50, v/v). The samples were analyzed by LC-MS/MS. Chromatographic separation was performed on an ACQUITY BEH C18 column (1.7 μM, 150 mm × 2.1 mm), using water (solvent A) and acetonitrile (solvent B) as mobile phases. The separation was achieved by a gradient elution as follows: 0 to 8 min, 29% B; 8 to 11 min, 29 to 85% B; 11 to 13 min, 95% B; 13 to 20 min, 29% B for re-equilibration. The method used positive ESI mode. The MRM transitions of R-2-HG derivative and S-2-HG-D5 derivative were m/z 387.2 → m/z 105 and m/z 392.2 → m/z 105, respectively. The retention time of the analyte and the internal standard was 7.99 min and 8.47 min, respectively.

Immunohistochemistry analysis
Tumor tissues were fixed with 4% paraformaldehyde immediately after mice were sacrificed. Subsequent immunohistochemistry analysis was performed by Shanghai Zuocheng Biological Technology. Images of sections were captured with NanoZoomer S210 (Hamamatsu, Japan) and further analyzed using NDP.View 2 software. The blood vessel density was analyzed by Aperio ImageScope software using the Microvessel Analysis v1 algorithm under default settings and the blood vessel numbers were normalized by the area of tumor sections for quantification.

Immunohistofluorescence staining
Tumor tissue samples were placed in 4% paraformaldehyde immediately after mice were sacrificed. Immunohistofluorescence staining was performed by Shanghai Zuocheng Biological Technology. Images of sections were captured using a laser scanning confocal microscope (Leica TCS-SP8 STED) with a HC APO L 100×/1.40 oil objective (Leica) at room temperature and further analyzed using ImageJ software. For pericyte coverage, the percentage of α-SMA and CD31-dual positive blood vessels over the total number of CD31-positive blood vessels were counted. Vascular perfusion was visualized by injecting 1.2 mg of FITC-conjugated lectin (#L0401, Sigma) into mice tail vein 3 min prior to tumor collection. The ratios of CD31 and FITC-lectin dual-positive blood vessels to the total CD31-positive blood vessels were examined to assess blood vessel perfusion. The basement membrane of blood vessels was stained with anti-Collagen IV antibody. The thickness of basement membrane was analyzed by the Local Thickness plugin of ImageJ. The Hypoxyprobe-1 Kit (#HP1, Hypoxyprobe) was used to detect tumor hypoxia by staining pimonidazole-protein adducts.

Blood flow by full-field laser perfusion imager
Mice were anaesthetized with Zoletil (intraperitoneally) and tumor blood flow was assessed using the Full-Field Laser Perfusion Imager (FLPI, Moor) and analyzed according to the manufacturer's instruction.

RNA fluorescence in situ hybridization (FISH)
Paraffin sections of tumor tissues were hybridized with CD31 and SLC1A1-specific fluorescence RNA probe mixes. RNA FISH was performed using RNA FISH Kit (GenePharma) according to the manufacturer's instructions. RNA probe sequences are as follows:

CD31 probe #1: Cy3-5′- CATCGTCCTTATAGAACAGCACCCG -3′;
CD31 probe #2: Cy3-5′- CACCTCGTACTCAATCGTGGTTTTT -3′;
CD31 probe #3: Cy3-5′- GAGAACTCTAACTTCGGCTTGGGAAAC -3′;
SLC1A1 probe #1: FAM-5′- TCACCTCTTCCCGCTTGGTTTTGTA -3′;
SLC1A1 probe #2: FAM-5′- AATCCAGTGCAGCGACACCTGTGA -3′;
SLC1A1 probe #3: FAM-5′- AGTACAGGCCCACGATCTTGTATTCCTT -3′.

Cell transfection
For plasmid transfection, cells were plated at 60%–70% confluence and transfected with indicated plasmids using Lipofectamine 3000 Transfection Reagent (#L30000015, Invitrogen) according to the manufacturer's instructions.

Lentivirus transduction
For the construction of SLC1A1-knockdown HUVECs, lentiviral particles containing indicated shRNAs targeting SLC1A1 were ordered from OBiO Technology and transduced into HUVECs following the manufacturer's instruction. Sequences used in this study were as follows:

Scramble: 5′- TTCTCCGAACGTGTCACGT -3′;
shSLC1A1 #1: 5′- GCATTACCACAGGAGTCTT -3′;

shSLC1A1 #2: 5′- GCAATCCACTCCATTGTAA -3′;
shSLC1A1 #3: 5′- GGATCACTCGATTCGTGTT -3′.

For the construction of HUVECs stably expressing 4mt-GCaMP6 and 4mt-ATeam1.03, the plasmids were transfected into 293T cells along with pSPAX2 and pMD2.G at a ratio of 4:3:1, respectively. HUVECs were transduced with lentivirus containing 4mt-GCaMP6 or 4mt-ATeam1.03 for 48 h and then subjected to time-lapse fluorescence analysis.

pSPAX2 (#12260) and pMD2.G (#12259) plasmids were purchased from Addgene. 4mt-GCaMP6 and 4mt-ATeam1.03 plasmids were gifts from Prof. Xin Pan (National Center of Biomedical Analysis, Beijing, China).

In silico molecular docking of SLC1A1
An electron microscopy structure of SLC1A1 in complex with TFB-TBOA has been released (PDB code: 6S3Q). However, this structure was not suitable for studying the binding of R-2-HG due to the difference between TFB-TBOA and R-2-HG. Thus, the models of SLC1A1 were built based on the structures of a homolog, SLC1A5. The reported two structures of SLC1A5 (PDB ID: 6MPB, 6GCT)[25,26] represented the outward-occluded and inward-occluded states of the transporter family, respectively. SLC1A5 is homologous to SLC1A1 with a sequence similarity of 42%. Therefore, the crystal structures of SLC1A5 were chosen as templates for the homology modeling. A sequence alignment was generated using the Clustal Omega server. The HP1-HP2 pocket is highly conserved among the SLC1 transporter family.[65] The binding models of R-2-HG to SLC1A1 were obtained using molecular docking. Docking and scoring were performed using the Schrodinger Glide software in InducedFit mode with default parameters.

Transwell migration assay
Transwell migration was performed in 24-well transwell plates with 8-μm pore-size chambers (Corning, USA). 2×10^4 HUVECs or HRECs were seeded in 100 μL of serum-free ECM into the upper chamber, and 600 μL ECM containing 5% FBS was added into the lower chamber, followed by an incubation at 37 °C in a 5% CO_2 incubator for 24 h. After removing the medium, the migrated cells were then fixed by 4% paraformaldehyde, stained with 0.5% crystal violet and photographed. The number of cells stained on the lower side of the well were counted. The relative migration (fold) was the fold change of migrated cell numbers versus the corresponding control group.

Wound-healing assay
HUVECs were seeded in 96-well plates overnight. Cells were treated with R-2-HG at indicated concentrations for 1 h and then scratched using a manual scratch tester (ESSEN Bioscience, USA). Subsequently, the cells were washed twice with PBS and then cultured in 100 μL serum-free medium containing R-2-HG at indicated concentrations. The cell culture plates were placed into the live-cell analysis system IncuCyte® (Essen BioScience Ltd., Hertfordshire, UK) to automatically captured scratches at 0 h and 6 h. Scratch width was further analyzed by ImageJ software. The wound-healing rate was calculated using the following formula to demonstrate the cell migration ability: Wound-healing rate = (0 h scratch width − 6 h scratch width)/0 h scratch width ×100%.

Tube formation assay
Matrigel (#3432-005-01, R&D System) was melted on ice, and 60 μL of matrigel was placed into the wells of a 96-well plate. The matrigel was polymerized at 37 °C for 30 min. HUVECs pre-treated with serum starvation for 6–8 h were harvested and resuspended using ECM containing 5% serum or indicated conditioned medium and then seeded into the matrigel-coated wells. Subsequently, cells were treated as indicated and incubated at 37 °C for another 6 h. The images of tube structure were captured using an inverted light microscope (IX73, Olympus) and analyzed using ImageJ software.

Aortic ring sprouting assay
Carotid arteries extracted from rats were carefully dissected from surrounding tissues and cut into rings and then placed in a pre-cooled matrigel (#3432-005-01, R&D System). The matrigel-ring mixture was covered with 100 μL Medium 199 (#11150067, Gibco) containing 100 ng/μL VEGF (#100-20, Peprotech) and subsequently treated as indicated for 7 days. DL-TBOA (#1223/10) and CGP-37157 (#HY-15754) were purchased

from Tocris and MedChemExpress, respectively. Photographs of the selected areas were taken under a microscope. Semi-quantitative analysis of intensities was performed using ImageJ software.

In vivo vascular network forming assay

Matrigel was thawed on ice at 4 °C overnight. 2×10^6 RBE or 8×10^5 GL261 cells and 1×10^6 HUVECs were mixed in 500 μL of matrigel for implantation per mice. Matrigel mixture was injected subcutaneously into the flank area of nude mice. After 14 days, mice were sacrificed and the matrigel plugs were taken out and placed in 4% paraformaldehyde immediately. Immunohistofluorescence staining was performed by Shanghai Zuocheng Biological Technology. Images of sections were captured using a laser scanning confocal microscope (Leica TCS-SP8 STED) and further analyzed using ImageJ software.

Seahorse XF analysis

We hydrated the XF96 Sensor Cartridge with Seahorse XF Calibrant Solution (#103095-000, Agilent) in a non-CO$_2$ incubator at 37 °C overnight. HUVECs or HRECs were seeded into a Seahorse XF96 Cell Culture Microplate (Agilent, CA, USA) at 2×10^4 cells/well and cultured for 24 h.

For the glycolysis stress test assay, cells were treated with 10 mM R-2-HG for 1 h and then washed and cultured in the Seahorse XF base medium (#103334-100, Agilent) supplemented with glutamine (2 mM) for 1 h at 37 °C in a non-CO$_2$ incubator. Extracellular acidification rate (ECAR) was monitored while being sequentially adding 10 mM glucose, 1 μM oligomycin and 50 mM 2-deoxy-glucose from the Seahorse XF Glycolysis Stress Test Kit (#103020-100, Agilent) for evaluating the glycolysis ability.

For the mitochondrial stress test assay, cells were treated with R-2-HG for 1 h and then washed and cultured in the Seahorse XF base medium supplemented with glucose (10 mM), pyruvate (1 mM) and glutamine (2 mM) for 1 h at 37 °C in a non-CO$_2$ incubator. Oxygen consumption rate (OCAR) was monitored while being sequentially adding 2 μM oligomycin, 1 μM FCCP and 0.5 μM rotenone/antimycin from the Seahorse XF Cell Mito Stress Test Kit (#103015-100, Agilent) for evaluating the mitochondrial respiratory ability.

For the respiration chain coupling assay and electron flow assay, mitochondrial assay solution (MAS) was prepared in advance. MAS recipe: 220 mM mannitol, 70 mM sucrose, 10 mM KH$_2$PO$_4$, 5 mM MgCl$_2$, 2 mM HEPES, 1 mM EGTA and 0.2% (w/v) fatty acid free BSA. Cells were cultured in the MAS and permeabilized with 0.004% (w/v) digitonin (#D141, Sigma-Aldrich), followed by a treatment of R-2-HG (10 mM) for 1 h. Subsequently, OCR was monitored upon sequentially adding 2 mM ADP (#A5285, Sigma-Aldrich), 2 μM oligomycin (#MB5431, Meilunbio), 1 μM FCCP (#S8275, Selleck) and 4 μM antimycin A (#A8674, Sigma-Aldrich) for respiration chain coupling assay or sequentially adding 2 μM rotenone (#MB5842, Meilunbio), 10 mM succinate (#S3674, Sigma-Aldrich), 4 μM antimycin A and 10 mM/100 μM ascorbate (#A5960, Sigma-Aldrich)/tetramethyl-p-phenylenediamine (#39391, Sigma-Aldrich) for electron flow assay.

ECAR and OCAR were detected following the manufacturer's instructions with Seahorse XF96 Analyzer (Agilent, CA, USA).

Immunoblotting analysis

Protein lysis was separated using sodium dodecyl sulfate-polyacrylamide gel electrophoresis (SDS-PAGE), transferred into a nitrocellulose membrane (Immobilon-P, Millipore), and then blocked for 1 h with 5% BSA in 1× Tris-buffered saline with Tween-20 (TBST) (25 mM Tris, 150 mM NaCl, 2 mM KCl, pH 7.4, supplemented with 0.1% Tween-20). Membranes were immuno-blotted with primary antibodies overnight at 4 °C. After washing the membranes with TBST, membranes were blotted with horseradish peroxidase-conjugated anti-rabbit IgG (1:2000 dilution) or anti-mouse IgG (1:2000 dilution) antibodies for 1 h at room temperature. Blots were visualized by ImageQuant™ LAS 4000 (GE Healthcare, USA) according to the manufacturer's instructions. Octyl-R-2-HG was from Sigma-Aldrich (#SML2200).

Antibodies

The following antibodies were purchased from respective companies: anti-EAAC1 (JU39-69) (Invitrogen, #MA5-34614), anti-Phospho-VEGF Receptor 2 (Tyr1175) (Invitrogen, #MA5-15170), anti-DYKDDDDK Tag (D6W5B) (CST, #14793), anti-VEGF Receptor 2 (D5B1) (CST, #9698), anti-β-Actin (13E5) (CST, #4970), anti-GAPDH (14C10) (CST, #2118), anti-AKT (pan) (C67E7) (CST, #4691), anti-Phospho-AKT (Ser473) (D9E) (CST, #4060), anti-HIF-1α (D1S7W) (CST, #36169), anti-Di-Methyl-Histone H3 (Lys27) (D18C8) (CST, #9728), anti-

Tri-Methyl-Histone H3 (Lys9) (D4W1U) (CST, #13969), anti-Tri-Methyl-Histone H3 (Lys36) (D5A7) (CST, #4909), anti-α-SMA (CST, #19245), anti-CD31 (CST, #77699), anti-RSK1 p90 (Abcam, #32114), anti-RSK1 p90 (phospho S380) (Abcam, #32203), and anti-Collagen IV (Abcam, #ab6586).

Single-cell sequencing data analysis

Single-cell sequencing data of normal brain tissue were extracted from the Single Cell Portal database (https://singlecell.broadinstitute.org/). Scatter-plots of SLC1A1 expression in different cell types were produced based on tSNE coordinates, clustering information and gene expression matrix downloaded from Single Cell Portal.

Measurement of mitochondrial ROS and F-actin staining

For mitochondrial ROS staining, live cells were first stained with 1 μM MitoSox Red (#M36008, Invitrogen) for 10 min at 37 °C and then fixed with 4% paraformaldehyde for 15 min. For F-actin staining, cells were fixed with 4% paraformaldehyde for 15 min and stained with 165 nM Alexa Fluor 488-phalloidin (#A12379, Invitrogen) for 10 min at room temperature. Cell nuclei were stained with DAPI (#C1002, Beyotime) for 10 min. Metformin (#MB1927) and Cytochalasin B (#MB5434) were purchased from Meilunbio. Images were captured using a laser scanning confocal microscope (Fluoview FV1000) with a UPlansApo 100×/1.40 oil (Olympus) at RT and processed using an FV1000 Viewer. Fluorescence intensity of MitoSox Red and Alexa Fluor 488-phalloidin were measured using ImageJ software.

For time-lapse analysis of F-actin formation, cells were cultured in imaging buffer (phenol red-free DMEM) and pre-incubated with CellMask Green Actin Tracking Stain (#A57243, Invitrogen) for 30 min at 37 °C according to the manufacturer's instructions. Images of F-actin were captured using a DeltaVision Ultra High Resolution Microscope (Cytiva) equipped with a 60×/1.42 NA objective. For imaging, exposure time was set to 20 ms for F-actin in green channel. Images were acquired at 1 frame per min.

Na$^+$ measurement

HUVECs were cultured in imaging buffer (phenol red-free DMEM) and pre-incubated with 5 μM CoroNa Green (#C36676, Invitrogen) for 15 min at 37 °C according to the manufacturer's instructions. Images of Na$^+$ were captured using a laser scanning confocal microscope (Fluoview FV1000) with a UPlansApo 100×/1.40 oil (Olympus) at RT and processed using an FV1000 Viewer and further analyzed using ImageJ software.

Ca^{2+} measurement

For imaging mitochondrial Ca^{2+} transients, HUVECs stably expressing 4mt-GCaMP6 were cultured in imaging buffer (phenol red-free DMEM) and pre-incubated with 50 nM MitoTracker Red CMXRos (#M7512, Invitrogen) for 15 min at 37 °C. Ca^{2+} imaging was then performed using a DeltaVision Ultra High-Resolution Microscope (Cytiva) equipped with a 60×/1.42 NA objective. For imaging, exposure time was set to 60 ms for 4mt-GCaMP6 in green channel and 5 ms for MitoTracker Red CMXRos in orange channel. Images were acquired at 2 frame per min.

For imaging cytosolic Ca^{2+} transients, HUVECs were cultured in imaging buffer (phenol red-free DMEM) and pre-incubated with 1 μM Fluo-4 (#F14201, Invitrogen) and 2.5 mM probenecid (#HY-B0545, MedChemExpress) for 30 min at 37 °C and then washed in PBS to remove any dye, followed by an incubation at 37 °C for a further 30 min before fluorescence measurements. For cytosolic Ca^{2+} imaging, expo-sure time was set to 18 ms for Fluo-4 in green channel. Images were acquired at 2 frame per minute.

For co-imaging of mitochondrial Ca^{2+} and mitochondrial ATP levels, HUVECs stably expressing 4mt-ATeam1.03 were cultured in imaging buffer (phenol red-free DMEM) and pre-incubated with 2.5 μM Rhod-2 (#R1245MP, Invitrogen) for 30 min at 37 °C and then washed in PBS to remove any dye, followed by an incubation at 37 °C for a further 60 min before fluorescence measurements. For mitochondrial Ca^{2+} imaging, exposure time was set to 4 ms for Rhod-2 in red channel. Images were acquired at 2 frame per min.

For image analysis, background correction was firstly performed frame by frame by subtracting the intensity of a nearby cell-free region from the signal of the imaged cell. F_0 is calculated as the initial background-subtracted fluorescence intensity. F indicates the background-subtracted fluorescence intensity at each time point. $\Delta F/F = (F - F_0)/F_0$ indicates the Ca^{2+} concentration change during the time after indicated treatment.

Mitochondrial ATP level imaging

HUVECs stably expressing 4mt-ATeam1.03 were cultured in imaging buffer (phenol red-free DMEM) and then visualized with a DeltaVision Ultra High-Resolution Microscope equipped with a 60×/1.42 NA objective. For imaging, 438/24 nm excitation filter and two emission filters (474/24 nm) for cyan fluorescent protein (CFP channel) and 548/22 nm for yellow fluorescent protein (YFP channel) were used. Exposure time was set to 50 ms and images were acquired (2 frames per min).

Image analysis was performed using ImageJ software. Background correction was performed frame by frame by subtracting the intensity of a nearby cell-free region from the signal of the imaged cells. The relative ATP levels were determined by (Fy–Fyb)/(Fc–Fcb). Fy and Fc indicate the YFP and CFP fluorescence intensity at each time point, respectively. Fyb and Fcb indicate the background intensity in the YFP and CFP channel, respectively.

NADH measurement

NADH level was measured using NAD^+/NADH Assay Kit with WST-8 (#S0175, Beyotime) following the manufacturer's instructions.

Cell motility, lamellipodia formation and mitochondrial motility assay

Sparse HUVEC cultures were assessed for spontaneous motility after plating on 35 mm-glass-bottom dishes (#M03-0401, Labtide). HUVECs were pre-incubated with 50 nM MitoTracker Red CMXRos for 15 min at 37 °C to track cell movement and monitor mitochondrial dynamics. The area of lamellipodia was measured by differential interference contrast (DIC) imaging. Images were acquired at intervals of 1 min for 4 h at 37 °C using a DeltaVision Ultra High-Resolution Microscope (objectives: 20× with NA 0.45). Exposure time was set to 46 ms in orange channel for MitoTracker Red CMXRos and 28 ms in DIC channel. Mitochondrial dynamics and lamellipodia area were analyzed using ImageJ software. Cell movement was tracked using ImageJ software by tracking mitochondrial position over time using TrackMate plugin with downsample LoG detector.

Mitochondria isolation

Mitochondria isolation was performed as previously reported.[37] Cells stably expressing Mito-2Strep were treated with doxycycline (1 μg/mL) for 48 h before replaced with fresh medium. Cells were washed twice with PBS and then collected in KPBS (136 mM KCl, 10 mM KH_2PO_4, pH 7.3). After centrifuged for 1 min at $1000 \times g$, cells were resuspended in 1 mL of KPBS and then homogenized. The homogenates were centrifuged at $1000 \times g$ for 2 min and the supernatant was incubated with pre-washed streptavidin-conjugated magnetic beads for 15 min at 4 °C. After incubation, the beads were washed with KPBS three times. After the final wash, mitochondria on the beads were eluted with 80% methanol or 2% SDS.

IDH enzymatic assay

IDH enzymatic activity was analyzed using the diaphorase/resazurin-coupled system. Recombinant human wild-type IDH1 (#14131) and IDH1-R132H (#14132) proteins were purchased from Cayman Chemical Company (Michigan, USA). Recombinant human IDH2-R140K (#31616), IDH2-R172K (#31618) and wild-type IDH2 (#31615) proteins were purchased from Active Motif, Inc. (Carlsbad, USA). Recombinant human IDH2-R140Q protein (#71100) was purchased from BPS Bioscience, Inc. (San Diego, USA). Recombinant human IDH1-R132C/G/S/L proteins were purified in our laboratory. The primary reaction was performed in a volume of 10 μL 1× buffer (150 mM NaCl, 20 mM Tris pH 7.5, 10 mM $MgCl_2$, 0.05% (w/v) bovine serum albumin) that contained IDH enzymes, 1 mM α-KG, 4 μM NADPH and the tested compounds for 60 min at 37 °C. To perform the secondary reaction, 5 μL of 1× buffer containing 0.01-unit diaphorase and 15 μM resazurin were added to the primary reaction and incub°Ced for a further 10 min at 25 °C. Fluorescence was read on a Spectramax plate reader at Ex 544/Em 590.

Purification of recombinant human IDH1-R132C/G/S/L proteins

The sequences coding human IDH1-mutant proteins were cloned into pET28a vector with an N-terminal TEV cleavable 6× His tag. The plasmids were transformed into *E. coli* BL21(DE3) cells and cultured at 37 °C in LB medium containing 50 mg/L kanamycin. 400 mM Isopropyl β-D-Thiogalactoside was added at 16 °C for 14–16 h. Bacterium were lysed by

sonication in buffer containing 25 mM Tris·HCl (pH 7.4) and 200 mM NaCl, and then centrifuged by a superfast centrifuge (18000 rpm, 45 min). The supernatant was collected for further purification using nickel affinity chromatography (His, Trap HP, GE Healthcare), followed by the gel-filtration chromatography on a Superdex 75 10/300 column (GE Healthcare).

Microscale thermophoresis (MST) assay

MST assay was conducted on Monolith NT.115 (NanoTemper) at room temperature. IDH1-R132C protein was diluted to 50 nM in MST buffer (25 mM HEPES pH7.4, 150 mM NaCl, 0.05% Tween) and labeled with the Monolith His-Tag Labeling kit RED-tris-NTA 2nd Generation (NanoTemper). IDH1-R132C was incubated with compounds at room temperature for 10 min and the signals were determined at 14% (Auto-detect) Pico-RED with Medium MST power. The Kd values were determined by Kd fitting model in the MO. affinity Analysis software v2.3 (NanoTemper) and the curves were plotted in the GraphPad prism 7.0.

Human sample datasets analysis

Mutation frequency of different IDH1 mutants in intrahepatic cholangiocarcinoma was obtained from MSK datasets through cBioPortal. Data of IDH1 mutation frequency, protein level of CD31 in 283 low grade glioma (LGG) samples were extracted from TCGA through cBioPortal database. For survival analysis, patients were divided into CD31 high- and CD31 low-groups by the median of *CD31* mRNA level.

TMT-labeled proteomics experiment

Tissues were lysed with lysis buffer (8 M urea, 100 mM NH_4HCO_3 and 10% v/v protease inhibitor). Protein concentration was determined using BCA assay. The protein-cysteine residues were reduced with 5 mM dithiothreitol at 56 °C for 30 min, and alkylated with iodoacetamide in the dark at room temperature for 30 min. The alkylation was quenched by adding another 5 mM dithiothreitol and incubated for 30 min at room temperature. Each protein solution was digested by sequence grade Lys-C enzyme at an enzyme-to-protein ratio of 1:100 (w/w) at 37 °C for 3 h. Then the protein solution was subjected to a 4-fold dilution with 100 mM NH_4HCO_3 and digested by sequence grade trypsin enzyme at an enzyme-to-protein ratio of 1:50 (w/w) at 37 °C for 16 h. The tryptic peptides were desalted through SepPak C18 cartridges and vacuum-dried before TMT labeling. TMT labeling was performed according to the manual description. All the TMT-labeled samples were pooled at 1:1 (w/w) ratio and subsequently vacuum-centrifuged to dry. The TMT-labeled peptides mixture was then desalted by Sep-Pak C18 cartridges. TMT-labeling efficiency was analyzed before deep proteome profiling. 10 μg TMT-labeled peptides were extracted and analyzed by Easy-nanoLC 1000 system tandem with Orbitrap Fusion mass spectrometer. The mass spectrometry data were converted into MGF format and searched by Mascot search engine against the UniProt human and mouse proteome database. Search parameters were as follows. Precursor ion peaks were searched with an initial mass tolerance of ±10 ppm, fragment mass tolerance of ±0.02 Da. Enzyme specificity with trypsin/P was used. Up to two missed cleavages were allowed. Carbamidomethylation of cysteine was set as a fixed modification. The oxidation of methionine, acetylation of protein N-terminus and TMT label on lysine and peptide N-terminus were set as variable modifications. The peptides score was cut off at 20.

RNA-seq analysis

RNA-seq analysis was conducted by Beijing Novogene Technology. In brief, total RNAs were extracted and RNA-seq libraries were prepared using Illumina RNA-Seq Preparation Kit and sequenced by an Ilumina Hiseq sequencer. RNA-seq reads were mapped using Hisat2 with default settings. Transcript assembly and transcript abundance quantification were carried out using featureCounts. Differential expression analysis was performed using DESeq2 R package.

Statistical analysis

Data were expressed as means ± SEM. Statistical significance was determined using one-way ANOVA with Dunnett multiple-comparisons test post hoc or Student's *t*-test as appropriate. Log-rank test was conducted for survival analysis. Differences were considered to be statistically significant at $P < 0.05$. Statistical calculations were performed with GraphPad Prism.

REFERENCES

1. Mardis, E. R. et al. Recurring mutations found by sequencing an acute myeloid leukemia genome. *N. Engl. J. Med.* **361**, 1058–1066 (2009).
2. Parsons, D. W. et al. An integrated genomic analysis of human glioblastoma multiforme. *Science* **321**, 1807–1812 (2008).
3. Yan, H. et al. IDH1 and IDH2 mutations in gliomas. *N. Engl. J. Med.* **360**, 765–773 (2009).
4. Borger, D. R. et al. Frequent mutation of isocitrate dehydrogenase (IDH)1 and IDH2 in cholangiocarcinoma identified through broad-based tumor genotyping. *Oncologist* **17**, 72–79 (2012).
5. DiNardo, C. D. et al. Durable remissions with ivosidenib in IDH1-mutated relapsed or refractory AML. *N. Engl. J. Med.* **378**, 2386–2398 (2018).
6. Tateishi, K. et al. Extreme vulnerability of IDH1 mutant cancers to NAD+ depletion. *Cancer Cell* **28**, 773–784 (2015).
7. Waitkus, M. S. & Yan, H. Targeting isocitrate dehydrogenase mutations in cancer: emerging evidence and diverging strategies. *Clin. Cancer Res.* **27**, 383–388 (2021).
8. Moure, C. J. et al. CRISPR editing of mutant IDH1 R132H induces a CpG methylation-low state in patient-derived glioma models of G-CIMP. *Mol. Cancer Res.* **17**, 2042–2050 (2019).
9. Mellinghoff, I. K. et al. Ivosidenib in isocitrate dehydrogenase 1-mutated advanced glioma. *J Clin Oncol.* **38**, 3398–3406 (2020).
10. Abou-Alfa, G. K. et al. Ivosidenib in IDH1-mutant, chemotherapy-refractory cholangiocarcinoma (ClarIDHy): a multicentre, randomised, double-blind, placebo-controlled, phase 3 study. *Lancet Oncol.* **21**, 796–807 (2020).
11. Dang, L. et al. Cancer-associated IDH1 mutations produce 2-hydroxyglutarate. *Nature* **462**, 739–744 (2009).
12. Lu, C. et al. IDH mutation impairs histone demethylation and results in a block to cell differentiation. *Nature* **483**, 474–478 (2012).
13. Xu, W. et al. Oncometabolite 2-hydroxyglutarate is a competitive inhibitor of alpha-ketoglutarate-dependent dioxygenases. *Cancer Cell* **19**, 17–30 (2011).
14. M Gagné, L., Boulay, K., Topisirovic, I., Huot, M. E. & Mallette, F. A. Oncogenic activities of IDH1/2 mutations: from epigenetics to cellular signaling. *Trends Cell Biol.* **27**, 738–752 (2017).
15. Friedrich, M. et al. Tryptophan metabolism drives dynamic immunosuppressive myeloid states in IDH-mutant gliomas. *Nat. Cancer* **2**, 723–740 (2021).
16. Bunse, L. et al. Suppression of antitumor T cell immunity by the oncometabolite (R)-2-hydroxyglutarate. *Nat. Med.* **24**, 1192–1203 (2018).
17. Rohle, D. et al. An inhibitor of mutant IDH1 delays growth and promotes differentiation of glioma cells. *Science* **340**, 626–630 (2013).
18. Folkman, J. Tumor angiogenesis: therapeutic implications. *N. Engl. J. Med.* **285**, 1182–1186 (1971).
19. Folkman, J. Role of angiogenesis in tumor growth and metastasis. *Semin. Oncol.* **29**, 15–18 (2002).
20. Seok, J., Yoon, S. H., Lee, S. H., Jung, J. H. & Lee, Y. M. The oncometabolite d2hydroxyglutarate induces angiogenic activity through the vascular endothelial growth factor receptor 2 signaling pathway. *Int. J. Oncol.* **54**, 753–763 (2019).
21. Potente, M., Gerhardt, H. & Carmeliet, P. Basic and therapeutic aspects of angiogenesis. *Cell* **146**, 873–887 (2011).
22. Gentile, M. T., Pastorino, O., Bifulco, M. & Colucci-D'Amato, L. HUVEC tube-formation assay to evaluate the impact of natural products on angiogenesis. *J. Vis. Exp.* https://doi.org/10.3791/58591 (2019).
23. Ye, J. L. et al. EAAT3 promotes amino acid transport and proliferation of porcine intestinal epithelial cells. *Oncotarget* **7**, 38681–38692 (2016).
24. Ximerakis, M. et al. Single-cell transcriptomic profiling of the aging mouse brain. *Nat. Neurosci.* **22**, 1696–1708 (2019).
25. Yu, X. et al. Cryo-EM structures of the human glutamine transporter SLC1A5 (ASCT2) in the outward-facing conformation. *Elife* **8**, e48120 (2019).
26. Garaeva, A. A. et al. Cryo-EM structure of the human neutral amino acid transporter ASCT2. *Nat. Struct. Mol. Biol.* **25**, 515–521 (2018).
27. Heinzelmann, G. & Kuyucak, S. Molecular dynamics simulations of the mammalian glutamate transporter EAAT3. *PLoS ONE* **9**, e92089 (2014).
28. Jain, R. K. Normalization of tumor vasculature: an emerging concept in anti-angiogenic therapy. *Science* **307**, 58–62 (2005).
29. Mancuso, M. R. et al. Rapid vascular regrowth in tumors after reversal of VEGF inhibition. *J. Clin. Invest.* **116**, 2610–2621 (2006).
30. Zhao, S. et al. Glioma-derived mutations in IDH1 dominantly inhibit IDH1 catalytic activity and induce HIF-1alpha. *Science* **324**, 261–265 (2009).
31. Fu, X. et al. 2-Hydroxyglutarate Inhibits ATP Synthase and mTOR Signaling. *Cell Metab.* **22**, 508–515 (2015).
32. Qing, Y. et al. R-2-hydroxyglutarate attenuates aerobic glycolysis in leukemia by targeting the FTO/m(6)A/PFKP/LDHB axis. *Mol Cell.* **81**, 922–939.e9 (2021).
33. Achouri, Y. et al. Identification of a dehydrogenase acting on D-2-hydroxyglutarate. *Biochem. J.* **381**, 35–42 (2004).
34. Magi, S. et al. Physical and functional interaction of NCX1 and EAAC1 transporters leading to glutamate-enhanced ATP production in brain mitochondria. *PLoS ONE* **7**, e34015 (2012).
35. Magi, S. et al. Glutamate-induced ATP synthesis: relationship between plasma membrane Na+/Ca2+ exchanger and excitatory amino acid transporters in brain and heart cell models. *Mol. Pharmacol.* **84**, 603–614 (2013).
36. Piccirillo, S., Castaldo, P., Macri, M. L., Amoroso, S. & Magi, S. Glutamate as a potential "survival factor" in an in vitro model of neuronal hypoxia/reoxygenation injury: leading role of the Na(+)/Ca(2+) exchanger. *Cell Death Dis.* **9**, 731 (2018).
37. Xiong, J. et al. Rapid affinity purification of intracellular organelles using a twin strep tag. *J. Cell Sci.* **132**, jcs235390 (2019).
38. Pellerin, L. How astrocytes feed hungry neurons. *Mol. Neurobiol.* **32**, 59–72 (2005).
39. Castaldo, P. et al. Role of the mitochondrial sodium/calcium exchanger in neuronal physiology and in the pathogenesis of neurological diseases. *Prog. Neurobiol.* **87**, 58–79 (2009).
40. Minelli, A. et al. Cellular and subcellular localization of Na+-Ca2+ exchanger protein isoforms, NCX1, NCX2, and NCX3 in cerebral cortex and hippocampus of adult rat. *Cell Calcium* **41**, 221–234 (2007).
41. Gobbi, P. et al. Mitochondrial localization of Na+/Ca2+ exchangers NCX1-3 in neurons and astrocytes of adult rat brain in situ. *Pharmacol. Res.* **56**, 556–565 (2007).
42. Rizzuto, R., De Stefani, D., Raffaello, A. & Mammucari, C. Mitochondria as sensors and regulators of calcium signalling. *Nat. Rev. Mol. Cell Biol.* **13**, 566–578 (2012).
43. De Bock, K., Georgiadou, M. & Carmeliet, P. Role of endothelial cell metabolism in vessel sprouting. *Cell Metab.* **18**, 634–647 (2013).
44. Pollard, T. D. & Borisy, G. G. Cellular motility driven by assembly and disassembly of actin filaments. *Cell* **112**, 453–465 (2003).
45. De Bock, K. et al. Role of PFKFB3-driven glycolysis in vessel sprouting. *Cell* **154**, 651–663 (2013).
46. Li, S. et al. Transient assembly of F-actin on the outer mitochondrial membrane contributes to mitochondrial fission. *J. Cell Biol.* **208**, 109–123 (2015).
47. Lei, J. et al. Compound having mutant idh inhibitory activity, preparation method and use thereof, National Center for Biotechnology Information. PubChem Patent Summary for WO-2017162133-A1. https://pubchem.ncbi.nlm.nih.gov/patent/WO-2017162133-A1.
48. Saha, S. K. et al. Isocitrate dehydrogenase mutations confer dasatinib hypersensitivity and SRC dependence in intrahepatic cholangiocarcinoma. *Cancer Discov.* **6**, 727–739 (2016).
49. Choi, S. et al. Vandetanib inhibits growth of adenoid cystic carcinoma in an orthotopic nude mouse model. *Clin. Cancer Res.* **14**, 5081–5089 (2008).
50. Leyva-Illades, D., McMillin, M., Quinn, M. & Demorrow, S. Cholangiocarcinoma pathogenesis: Role of the tumor microenvironment. *Transl. Gastrointest. Cancer* **1**, 71–80 (2012).
51. Sirica, A. E. & Gores, G. J. Desmoplastic stroma and cholangiocarcinoma: clinical implications and therapeutic targeting. *Hepatology* **59**, 2397–2402 (2014).
52. Peraldo-Neia, C. et al. Transcriptomic analysis and mutational status of IDH1 in paired primary-recurrent intrahepatic cholangiocarcinoma. *BMC Genomics* **19**, 440 (2018).
53. Wang, P. et al. Mutations in isocitrate dehydrogenase 1 and 2 occur frequently in intrahepatic cholangiocarcinomas and share hypermethylation targets with glioblastomas. *Oncogene* **32**, 3091–3100 (2013).
54. Saha, S. K., Parachoniak, C. A. & Bardeesy, N. IDH mutations in liver cell plasticity and biliary cancer. *Cell Cycle* **13**, 3176–3182 (2014).
55. Saha, S. K. et al. Mutant IDH inhibits HNF-4alpha to block hepatocyte differentiation and promote biliary cancer. *Nature* **513**, 110–114 (2014).
56. Dong, L. et al. Proteogenomic characterization identifies clinically relevant subgroups of intrahepatic cholangiocarcinoma. *Cancer Cell* **40**, 70–87.e15 (2022).
57. Carbonneau, M. et al. The oncometabolite 2-hydroxyglutarate activates the mTOR signalling pathway. *Nat. Commun.* **7**, 12700 (2016).
58. Su, R. et al. R-2HG exhibits anti-tumor activity by targeting FTO/m(6)A/MYC/CEBPA signaling. *Cell* **172**, 90–105.e23 (2018).
59. Li, T. et al. D-2-Hydroxyglutarate is necessary and sufficient for isocitrate dehydrogenase 1 mutant-induced MIR148A promoter methylation. *Mol. Cancer Res.* **16**, 947–960 (2018).
60. Kim, G. H. et al. IDH1(R132H) causes resistance to HDAC inhibitors by increasing NANOG in glioblastoma cells. *Int. J. Mol. Sci.* **20**, 2679 (2019).
61. Chowdhury, R. et al. The oncometabolite 2-hydroxyglutarate inhibits histone lysine demethylases. *EMBO Rep.* **12**, 463–469 (2011).
62. Bailey, C. G. et al. Loss-of-function mutations in the glutamate transporter SLC1A1 cause human dicarboxylic aminoaciduria. *J. Clin. Invest.* **121**, 446–453 (2011).
63. Muhlhausen, C. et al. Membrane translocation of glutaric acid and its derivatives. *J. Inherit. Metab. Dis.* **31**, 188–193 (2008).
64. Jin, N. et al. Identification of metabolic vulnerabilities of receptor tyrosine kinases-driven cancer. *Nat. Commun.* **10**, 2701 (2019).

65. Boudker, O., Ryan, R. M., Yernool, D., Shimamoto, K. & Gouaux, E. Coupling substrate and ion binding to extracellular gate of a sodium-dependent aspartate transporter. *Nature* **445**, 387–393 (2007).

ACKNOWLEDGEMENTS

AUTHOR CONTRIBUTIONS

M.H. conceived the project and supervised the study; Z.C. initiated the project and discovered R-2-HG-promoted endothelial cell migration and mitochondrial activation; N.A. contributed to the early stage of SLC1A1 discovery; X.W. and J.X. established the role of SLC1A1 in R-2-HG uptake, discovered SLC1A1-dependent mitochondrial Na^+/Ca^{2+} exchange, and demonstrated the role of SLC1A1 in R-2-HG-promoted angiogenesis in vivo; S.T. characterized mIDH1 inhibitors; L.J. invented HH2301; Y. Zhang and L.L. supervised the preclinical development of HH2301 and verified HH2301 compound-related information; T.W., S.Cao., Y.Liu., A.B., Yuehong.C., X.G., Y.D. and Y.Zheng. performed part of experiments; Y.F., Y.Li., L.Y. and L.T. provided technique assistance; Qingli.Z., X.L. and J.L. conducted R-2-HG measurement; S.Chen, S.G., K.M., M.W. and C.L. purified IDH1 proteins and performed MST assay; S.-H.L. performed metabolome analysis; S.Z. and Qiansen.Z. did SLC1A1 molecular modeling and docking; Y.S. and Yi.C. performed part of PDX studies; L.Z. and M.T. performed proteomics analysis; X.W. and J.X. prepared all figures; M.H., X.W. and J.X. wrote the manuscript. All authors approved the final version of the manuscript.

COMPETING INTERESTS

ADDITIONAL INFORMATION

Supplementary information The online version contains supplementary material available at https://doi.org/10.1038/s41422-022-00650-w.

Correspondence and requests for materials should be addressed to Min Huang.

Reprints and permission information is available at http://www.nature.com/reprints